Ana Catarina Almeida Reis
Licenciada em Bioquímica

Development of novel drug delivery systems for cancer therapy

Dissertação para obtenção do Grau de Mestre em
Bioquímica

Orientador: Prof. Doutor Ilídio Joaquim Sobreira Correia, UBI
Co-orientador: Mestre André Ferreira Moreira, UBI

Júri:

Presidente: Prof. Doutor Carlos Alberto Gomes Salgueiro
Arguente: Prof. Doutor Ricardo Oliveira Louro
Vogal: Prof. Doutor Ilídio Sobreira Correia

FACULDADE DE CIÊNCIAS E TECNOLOGIA
UNIVERSIDADE NOVA DE LISBOA

Setembro 2018

LOMBADA

Development of novel drug delivery systems for cancer therapy
Ana Reis

2018

Ana Catarina Almeida Reis

Licenciada em Bioquímica

Development of novel drug delivery systems for cancer therapy

Dissertação para obtenção do Grau de Mestre em
Bioquímica

Orientador: Prof. Doutor Ilídio Joaquim Sobreira Correia, UBI
Co-orientador: Mestre André Ferreira Moreira, UBI

Júri:

Presidente: Prof. Doutor Carlos Alberto Gomes Salgueiro
Arguente: Prof. Doutor Ricardo Oliveira Louro
Vogal: Prof. Doutor Ilídio Sobreira Correia

Setembro
2018

Development of novel drug delivery systems for cancer therapy

“There are two great days in the person’s life:
the day we were born and the day we prove why we are born.
Best wishes for the second one!”

À minha mãe, avós e Rui, dedico esta tese.

Agradecimentos

Em primeiro lugar gostaria de agradecer ao meu orientador Professor Doutor Ilídio Correia pela oportunidade e por me ter aceite para integrar o seu grupo de investigação. A sua orientação, recomendações e exigência foram essenciais para o desenvolvimento desta dissertação e também para me ajudaram a crescer tanto a nível pessoal como profissional.

Ao meu co-orientador, André Moreira, agradeço por toda a ajuda, paciência e tempo despendido comigo ao longo desta etapa. Estou grata ainda pelo conhecimento que me transmitiu, a constante troca de ideias e sua boa disposição contagiante. Sem o seu apoio e orientação este trabalho não teria sido possível.

Aos meus colegas de grupo de investigação, agradeço o seu apoio incondicional, incentivo, a disponibilidade para ajudarem, boa disposição e bons momentos proporcionados. À Carolina, a minha parceira de laboratório, quero agradecer a sua ajuda que foi indispensável ao longo deste percurso e a sua paciência para me aturar. A todas as outras meninas do grupo, Cátia, Sol, Sofia, Déborah, Rita, que estavam lá todos os dias. Agradeço também ao Duarte, Beta e Sónia pela boa disposição diária e por me terem ajudado a embarcar nesta aventura.

Aos meus melhores amigos que estavam comigo diariamente nesta aventura, Raquel e Megs, agradeço a paciência para ouvirem os meus desabafos e o incentivo que me transmitiram nas alturas mais stressantes. Estes 5 anos juntas foram os melhores, cheios de histórias, aventuras, sorrisos e choradeiras, o que a faculdade junta nunca se irá separar. À Diana, que por mais longe que esteja fisicamente, tem sempre um espacinho no meu pensamento, um muito obrigada pelas aventuras que vivenciámos ao longo dos 12 anos da nossa amizade, sei que posso contar sempre contigo! E por fim, às minhas companheiras que a FCT juntou, Marina e Margarida, sem vocês teria sido impossível.

À minha família que esteve diariamente comigo, em especial a minha mãe Paula e avós. Sem a vossa paciência, amor e apoio não teria sido possível culminar esta etapa da minha vida. Obrigada por todos os conselhos, confiança e encorajamento. Ao meu pai Vitor e à Ilda, também um obrigada pela paciência e amor.

Finalmente, quero agradecer do fundo do coração ao meu namorado Rui, por ser o meu suporte ao longo destes anos, sem a sua paciência, amor e confiança não teria sido possível chegar a este dia. Obrigada por não me teres deixado desistir e por confiares em mim.

Resumo

O cancro é uma das principais causas de morte da população a nível mundial. Além disso, as abordagens terapêuticas atualmente utilizadas no tratamento desta doença são inespecíficas e ineficazes. Esta realidade enfatiza a importância de desenvolver novas terapias que possam ser usadas no tratamento desta patologia. Na área da nanotecnologia têm sido desenvolvidas novas ferramentas terapêuticas que têm revelado um elevado potencial para incrementar a esperança de vida dos pacientes. Os nanodispositivos desenvolvidos podem atuar simultaneamente como agentes terapêuticos e de imagem, o que permite a monitorização em tempo real da biodistribuição das nanopartículas e da sua eficácia terapêutica. Entre os diferentes tipos de nanopartículas, as nanopartículas de ouro com revestimento de sílica (AuMSS) apresentam propriedades físico-químicas e biológicas promissoras para a sua aplicação na terapia do cancro. No entanto, a disseminação das AuMSS na clínica tem sido limitada devido à sua baixa estabilidade coloidal, farmacocinética desfavorável e pela libertação descontrolada dos fármacos. Neste trabalho, um novo revestimento polimérico foi produzido para ser aplicado na superfície das nanopartículas esféricas de AuMSS. Para este propósito, realizou-se a funcionalização das AuMSS com diferentes rácios (25/75, 50/50 e 75/25) de dois polímeros, poli-2-etil-2-oxazolina (PEOZ) e β-ciclodextrinas (β-CD). O PEOZ foi selecionado devido à sua capacidade para aumentar a solubilidade e, consequentemente, a estabilidade coloidal destas nanopartículas. Por outro lado, a β-CD irá permitir o bloqueio dos poros das partículas e, consequentemente, controlar a libertação do fármaco neles encapsulado. Os resultados obtidos neste estudo revelaram que a funcionalização da superfície das nanoesferas de AuMSS com estes dois polímeros induziu um aumento no tamanho das nanopartículas, neutralizou a sua carga superficial, e incrementou a biocompatibilidade e a taxa de internalização destas nanopartículas pelas células cancerígenas do colo do útero (HeLa). Por outro lado, os resultados obtidos confirmam ainda que estes nanodispositivos têm potencial para aplicação na terapia do cancro, onde podem agir simultaneamente como agentes de entrega de fármacos e imagem.

Palavras-Chave

Cancro, Nanopartículas de ouro com Revestimento de Sílica, PEOZ, β-CD.

Abstract

Cancer is one of the major causes of death in the worldwide population. Such is explained by the nonspecificity and ineffectiveness of the currently available treatments. This reality highlights the importance of developing novel therapeutic approaches. Nowadays, multifunctional nanomedicines are revealing promising properties that can revolutionize cancer treatment, since they can act simultaneously as therapeutic and imaging agents allowing the real-time monitoring of the nanoparticles biodistribution and treatment efficacy. Amongst the different nanoparticles produced so far, the gold-core silica shell (AuMSS) nanoparticles display advantageous physicochemical and biological properties that make them promising nanoplatforms for cancer therapy. Nevertheless, their successful application is limited by the unfavorable pharmacokinetics and uncontrolled release of the therapeutic payloads. Herein, different polymeric ratios (25/75, 50/50 and 75/25) of Poly-2-ethyl-2-oxazoline (PEOZ) and β-cyclodextrin (β-CD) were combined to coat AuMSS nanospheres. The PEOZ was selected due to its capacity to improve the solubility and, consequently, the colloidal stability of the nanodevices. On the other side, the β-CD will block the AuMSS pores restraining the release of the therapeutic molecules encapsulated within the nanoparticles. The surface functionalization of AuMSS nanospheres induced a size increase of the nanoparticles, a neutralization of the surface charge, an enhanced biocompatibility and a higher internalization rate by the cervical cancer cells (HeLa). Overall, the obtained data confirm the successful modification of the AuMSS nanospheres with PEOZ and β-CD as well as their potential to be used as drug delivery and bioimaging agents for cancer therapy.

Keywords

Cancer, Gold core-silica shell nanoparticles, PEOZ, β-CD.

List of Publications

Moreira, A. F.*, Rodrigues, C. F.*, Reis, C. A.*, Costa, E. C., and Correia, I. J. (2018). “Gold-core silica shell nanoparticles application in imaging and therapy: A review.” Microporous and Mesoporous Materials. 270:168-179. DOI:10.1016/j.micromeso.2018.05.022.

Moreira, A. F., Rodrigues, C. F., Reis, C. A., Costa, E. C., Ferreira, P., and Correia, I. J. “Development of poly(2-ethyl-2-oxazoline) coated gold-core silica shell nanorods for the chemo-photothermal cancer therapy.” Nanomedicine. DOI:10.2217/nnm-2018-0179. Accepted for publication.

Rodrigues, C. F., Reis, C. A., Moreira, A. F., Ferreira, P., and Correia, I. J. “Optimization of gold core-mesoporous silica shell functionalization with TPGS and PEI for cancer therapy.” Submitted for publication.

Reis, C. A., Rodrigues, C. F., Moreira, A. F., Ferreira, P., and Correia, I. J. “Development of Gold-Core Silica Shell Nanospheres Coated with Poly-2-ethyl-oxazoline and Beta-cyclodextrin Aimed for Cancer Therapy.” Submitted for publication.

*These authors had an equal contribution to this article.

Index

Figure Index

List of Abbreviations

ANOVA	One-way analysis of variance
AR	Aspect ratio
ATP	Adenosine triphosphate
AuMSS	Gold core-silica shell
CLSM	Confocal laser scanning microscopy
CT	Computerized tomography
CTAB	Cetyltrimethylammonium bromide
DLS	Dynamic light scattering
DMEM-HG	Dulbecco's modified eagle medium-high glucose
DNA	Deoxyribonucleic acid
DOTA	1,4,7,10-tetraazacyclododecane-1,4,7,10-tetraacetic acid
DSPE	1,2-distearoyl-sn-glycero-3-phosphoethanolamine
ECM	Extracellular matrix
EDTA	Ethylenediamine tetraacetic acid
EPR	Enhanced permeability and retention
EtOH	Ethanol
FBS	Fetal bovine serum
FITC	Fluorescein isothiocyanate
FTIR	Fourier transform infrared
GSH	Glutathione
HeLa	Human negroid cervix epithelioid carcinoma
HepG2	Liver hepatocellular carcinoma
KRB	Krebs ringer buffer
MRI	Magnetic resonance imaging
NIR	Near-infrared
PA	Photoacoustic
PBS	Phosphate-buffered saline solution
PDT	Photodynamic therapy

PEG	Polyethylene glycol
PEOZ	Poly-2-ethyl-2-oxazoline
PNIPAM	Poly(Nisopropylacrylamide)
PTT	Photothermal therapy
RBC	Red blood cell
RES	Reticuloendothelial system
RGD	Arginyl-glycyl-aspartic acid
ROS	Reactive oxygen species
RVG29	29 Residue peptide derived from rabies virus glycoprotein
SERS	Surface enhanced Raman spectroscopy
SLN	Solid lipid nanoparticles
TEM	Transmission electron microscopy
TEOS	Tetraethyl orthosilicate
TESPIC	3-(Triethoxysilyl)propyl isocyanate
TGA	Thermogravimetric analysis
THF	Tetrahydrofuran
T-PEOZ	TESPIC-PEOZ
T-β-CD	TESPIC-β-CD

List of Symbols

D	Translation diffusion coefficient
f(Ka)	Henry's equation
K_B	Boltzmann's constant
r	Hydrodynamic diameter
T	Thermodynamic temperature
U_E	Electrophoretic mobility
β-CD	Beta-cyclodextrin
ε	Dielectric constant
ζ	Zeta potential
η	Dynamic viscosity

Chapter 1

Introduction

This chapter is based on the publication entitled: “Gold-Core Silica Shell Nanoparticles Application in Imaging and Therapy: a Review” (2018). Microporous and Mesoporous Materials. 270: 168-179 (DOI:10.1016/j.micromeso.2018.05.022)

1. Introduction

1.1. Cancer

1.1.1 Cancer statistics

Cancer is a major public healthcare issue, causing millions of deaths every year. The last global statistics for cancer (GLOBOCAN 2012) indicate that in 2012 around fourteen million new cases of cancer were diagnosed and more than eight million cancer-related deaths occurred (1). In the current year, Siegel *et al.* estimate that more than one million seven hundred thousand new cases will be diagnosed and more than six hundred thousand cancer-related deaths will occur only in the United States of America (2). In 2017, the *Direção Geral de Saúde* reported that in Portugal, the cancer incidence has been increasing at a rate of 3% per year since 1995. Further, the report also predicts that in 2035, sixty thousand new cases of cancer will be diagnosed and that this disease will be responsible for thirty thousand deaths (3). These alarming numbers reported for cancer are associated with several risk factors such as exposition to environmental agents (*e.g.* radiation and pollution), lifestyle (*e.g.* tobacco, alcohol, and drugs) as well as genetic predisposition. Also, the cancer prevalence has been reported as being dependent on gender and patient age (Figure 1.1) (4, 5).

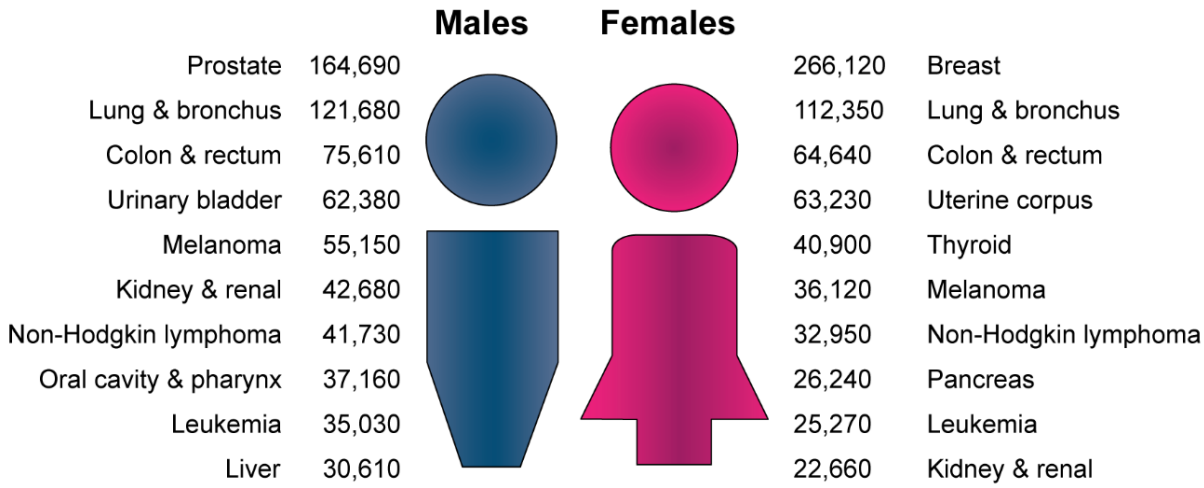

Figure 1.1. Representation of the ten types of cancer with higher incidence by gender in the United States of America. Data is estimated for 2018. Adapted from (2).

1.1.2 Cancer hallmarks

Cancer can be defined as a group of different diseases that share several key characteristics and are capable of affecting the various organs of the human body (5). Cancer was initially described as a mass of cancer cells that display a continuous and uncontrolled proliferation rate, as well as the capacity to invade the surrounding tissues or colonize other sites of the body (6, 7). Nowadays, cancer is described as a complex and heterogeneous tissue, where cancer cells interact with the surrounding stromal cells and non-cellular elements occur, the so-called tumor microenvironment (8). In the tumor

microenvironment, apart from cancer cells, are also found endothelial, pericytes, cancer-associated fibroblasts, immune system cells, extracellular matrix (ECM) compounds and signalling molecules (Figure 1.2) (9, 10). The establishment of cross-talk interactions between the tumor microenvironment elements plays a critical role in cancer progression, for example by triggering invasion, pro-survival and proliferation pathways (8, 9). Additionally, the complex interactions between the tumor microenvironment constituents allow the transformation of cancer cells, allowing them to acquire and maintain certain key characteristics denominated “hallmarks of cancer” (Figure 1.3) (6, 11).

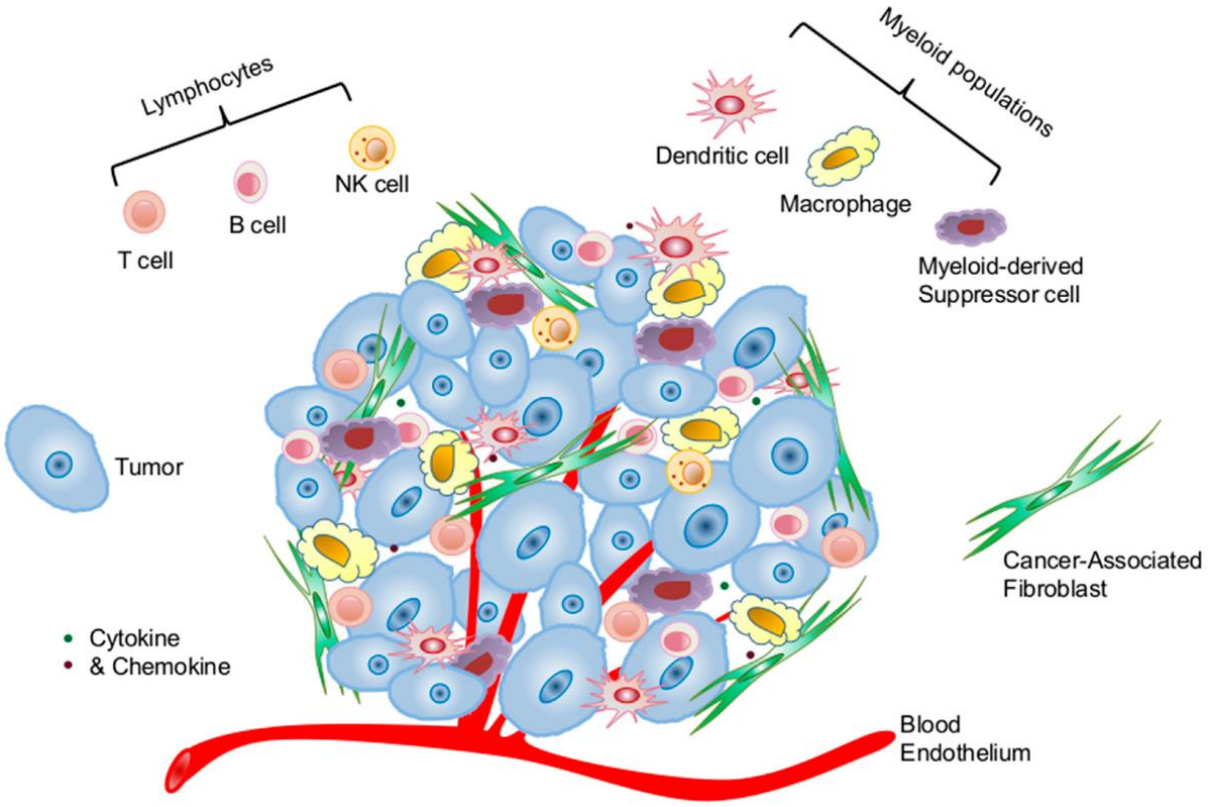

Figure 1.2. Representation of the tumor heterogeneity and complexity. The complex tumor microenvironment is characterized by the cross-talking between malignant, endothelial, pericytes, fibroblasts, and immune system cells, as well as with the extracellular matrix. Reproduced from (10).

One of the most important characteristics of cancer cells is their capacity to maintain the proliferation signalling independently of the surrounding tissues by producing their own growth signals (*e.g.* platelet-derived growth factor) or overexpressing receptors involved in cell growth pathways (6, 12). Furthermore, these cells also develop the capacity to avoid the programmed cellular death through the enhanced expression of anti-apoptotic proteins, such as B-cell lymphoma 2 family (13), as well as evade growth suppressors like protein 53 and retinoblastoma protein (11). Additionally, the cancer cells have a limitless replicative capacity through the overexpression of telomerase, an enzyme that adds repeated segments of hexanucleotides to the end of deoxyribonucleic acid (DNA). Therefore, the integrity of telomeres is maintained to prevent the DNA damage and the cell apoptosis or senescence. In normal cells, the telomerase expression is almost absent, resulting in a decreased capacity to conserve the

telomeres throughout the successive replicative cycles leading, ultimately, to cell death (6, 14). Moreover, cancer cells also induce the angiogenesis to have access to oxygen and nutrients, as well as to remove the metabolic waste and carbon dioxide generated by their metabolism. For that purpose, cancer cells modulate the expression of angiogenesis inducers or inhibitors (*e.g.* vascular endothelial growth factor, fibroblast growth factor, platelet-derived growth factor, and angiopoietins are often overexpressed) (15, 16). Another hallmark of cancer cells is its capacity to extravasate, invade and colonize other tissues throughout the body (*i.e.* metastization) due to the deregulation of the expression of several proteins involved in cell-cell and cell-ECM adhesion. One example of this downregulation comprises the e-cadherin protein expression leading to the loss of the cell-cell adhesion and favoring the colonization of other tissues by the cancer cells (6, 17). Recently, it was also demonstrated that the cancer cells have the capacity to avoid the recognition and destruction by the immune system and to reprogram their metabolism in order to enhance the tumor proliferation and progression (6).

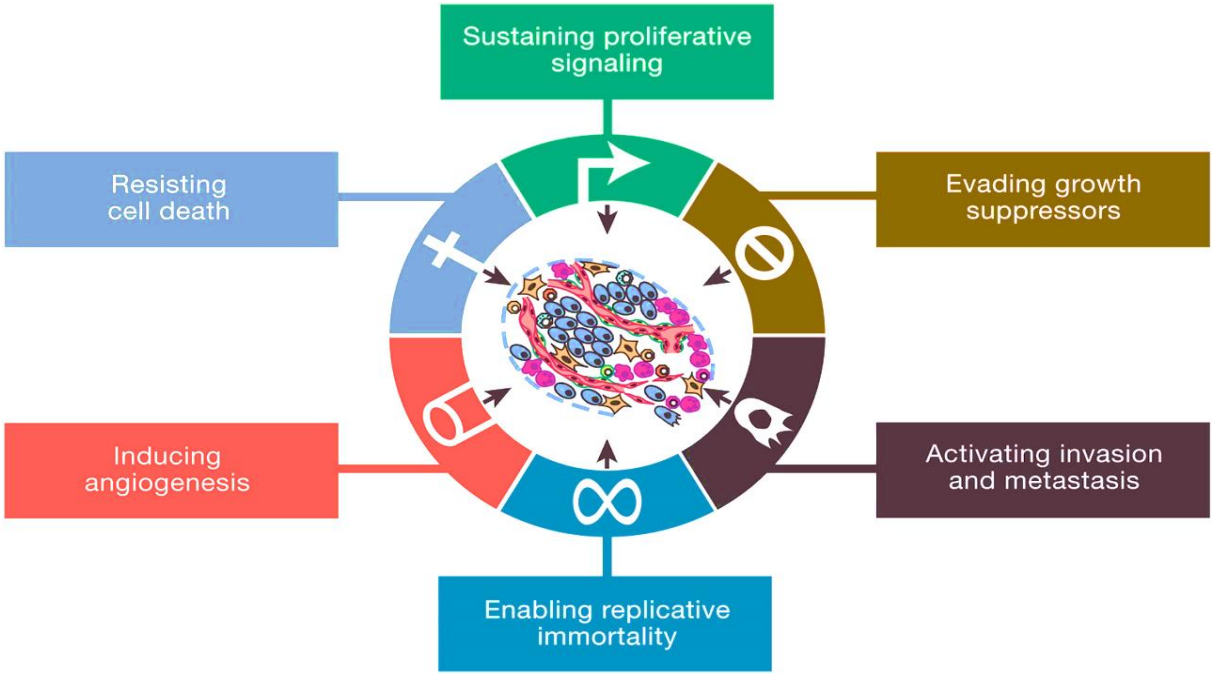

Figure 1.3. Summary of the cancer hallmarks that are responsible for the development, maintenance, and progression of cancer. Reproduced from (6).

1.1.3 Therapies

The cancer therapies commonly applied in the clinic include chemotherapy, radiotherapy, surgery and hormone therapy (18). Among them, the combination of surgery with chemotherapy and/or radiotherapy are the most common approaches employed for cancer treatment. However, these therapies are not specific to cancer cells and also induce damages in healthy cells resulting in side effects such as fatigue, nausea infertility, pain, organ failure or even death (6, 18).

Nowadays, chemotherapy remains as the first-line of treatment for cancer, however, its therapeutic efficacy is limited by the drugs weak bioavailability, low selectivity, reduced water solubility, rapid

degradation and short half-life in blood circulation (19, 20). In addition, cancer cells can acquire a multidrug resistance phenotype such as increased expression of membrane transporters involved in drug efflux, a mutation in the drug target, the repair of the damaged DNA and the downregulation of the cell death mechanisms. Moreover, the acquisition of a multidrug resistance phenotype by cancer cells in response to the administration of one therapeutic agent can also translate into an increased resistance to other therapeutic agents, even those with different chemical structure (21, 22). One of the most investigated multidrug resistance mechanism is the overexpression of membrane transporters that act as drug efflux pumps. The glycoprotein-P is a member of the adenosine triphosphate (ATP)-binding cassette transporters family, a group of transmembrane proteins that transport molecules to the exterior of the cell, at expense of ATP hydrolysis (22, 23). Therefore, the action of this efflux pump avoids the intracellular accumulation of anticancer drug impairing the therapeutics effectiveness (24).

1.2 Nanotechnology in cancer therapy

The recent advances in the area of nanotechnology have emerged as one of the most promising approaches for improving the currently available therapies (25). In fact, different nanomedicines are presently being employed for the diagnosis, monitoring, and treatment of several diseases such as cancer (26, 27), Alzheimer (28, 29) and Parkinson (30, 31). Particularly, in cancer therapy, the nanoparticles unique physicochemical properties and the capacity to transport and promote a specific drug delivery prompted their application has imaging, therapeutic or even theragnostic agents (32, 33). Over the years, the controlled drug delivery mediated by nanoparticles has progressed, as well as the nanoparticle requirements to be applied in the clinic. The first generation of drug delivery systems was produced by using simple materials and with the objective to promote a sustained drug release, by the process of dissolution, diffusion, osmose or ionic exchange. Subsequently, a second generation of the nanocarriers aimed to perform a stimuli-sensitive drug delivery as well as to promote a preferential accumulation of the drug within the tumor tissue. The third and actual generation is based on the production of drug delivery systems with smart materials that are able to perform long term delivery (*i.e.* over six months), fast response kinetics to *in vivo* stimulus and that are able to surpass the biological barriers to perform drug delivery (*e.g.* blood-brain barrier) (34).

1.2.1 Classes of nanoparticles

During the last years, researchers have been focused on the development of novel nanocarriers with the capacity to act as drug delivery system and/or imaging agents for cancer therapy. The nanoparticles can be classified into two major classes considering the raw material used in their synthesis: organic and inorganic nanoparticles (Figure 1.4). Within the organic nanostructures, there are two main classes, lipid-based and polymer-based nanoparticles.

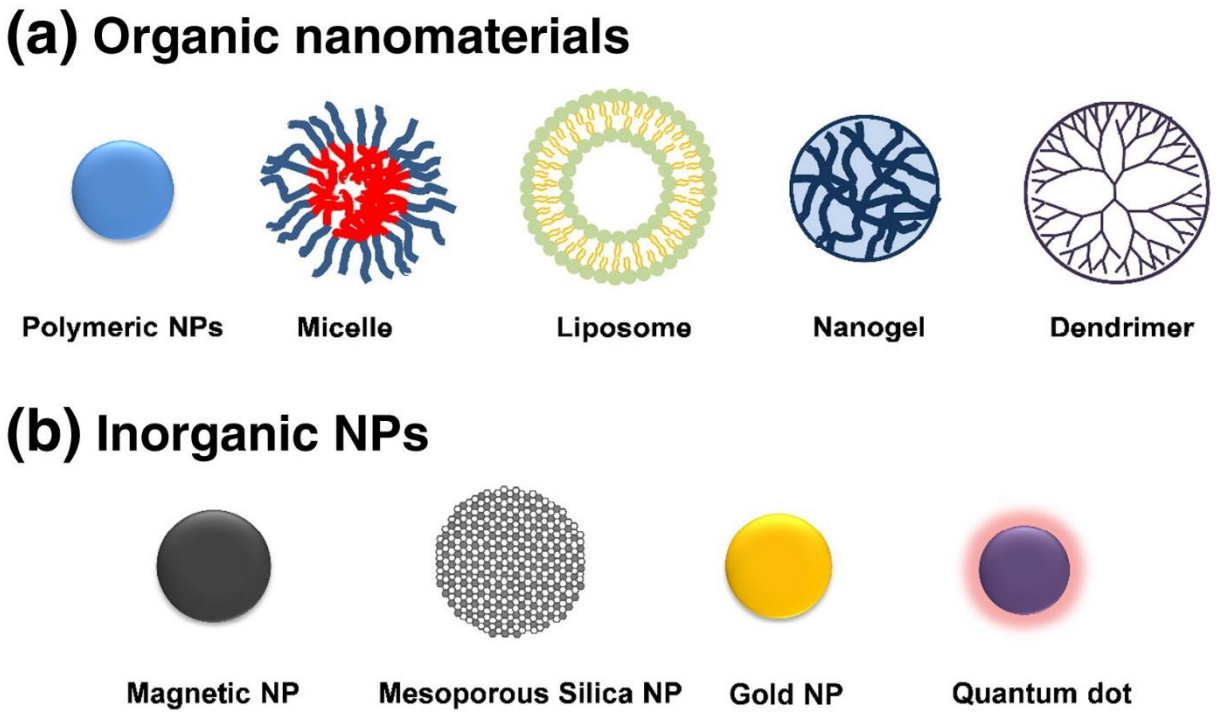

Figure 1.4. Representation of the different types of nanoparticles that can be produced with different materials and synthesis procedures. Reproduced from (35).

The lipid-based nanoparticles are usually produced with a liposome or lipidic micelle organization. The liposomes are composed by one or more phospholipid bilayers, that display a spherical organization and an aqueous core. This liposomal organization allows the transport of both water-soluble and hydrophobic drugs, in the water core or within the phospholipid bilayer. The Doxil® was the first liposome approved by the Food and Drug Administration, in 1995, for cancer therapy. This liposomal nanocarrier loaded with Doxorubicin was coated with polyethylene glycol (PEG) to improve its blood circulation time in the human body (36). On the other side, lipidic micelles are generally composed by a monolayer of phospholipids organized in a micellar structure. This type of nanoparticles is particularly valuable for the encapsulation of hydrophobic molecules, which are entrapped in their hydrophobic core. However, lipid-based systems display some disadvantages, such as limited stability, opsonization, and reduced control over the drug release, that hinder theirs *in vivo* application (37).

Solid lipid nanoparticles (SLNs) are an alternative lipidic sub-type made from solid lipids stabilized by surfactants and that are solid at the room and body temperature (38). SLNs can be produced with highly purified triglycerides (tricaprin, trilaurin, tripalmitin, and others), complex glyceride mixtures (glyceryl palmitostearatea and glyceryl monostearate) or even waxes (cetyl palmitate) (39). SLNs are formed by a solid hydrophobic core with an external layer of phospholipids (38). The lipophilic or hydrophilic bioactive compounds can be dissolved or dispersed in the solid matrix (40). The solid nanoparticle properties are mainly influenced by their lipid composition, production method and surfactant type (38). However, they present some advantages such as their composition (*i.e.* physiological compounds), high biocompatibility, and potential for large scale production (38). Furthermore, their content release can be modulated by using different loading process (41). On the other hand, these nanocarriers present some

disadvantages namely their low drug loading capacity and the presence of alternative colloidal structures (nanoparticles micelles, liposomes, and drug nanocrystals can also be formed) (38).

Among the polymer-based nanoparticles, polymeric micelles are one of the most used structures for drug delivery. These nanostructures are prepared using amphiphilic polymers and their organization allows the encapsulation of poorly water-soluble drugs on the micelle core, which is formed by the hydrophobic segment of the polymer. The polymeric hydrophilic shell is exposed to the solvent and it prevents the adsorption of plasma proteins and increases the nanoparticle blood circulation time (36, 42). Nanoplatin® is an example of a micellar structure that is currently under evaluation in clinical trials. This nanocarrier is composed of Cisplatin and a copolymer (PEG-polyglycolic acid) demonstrating a pharmacokinetic profile more advantageous than that displayed by free Cisplatin, which leads to a reduction of the cisplatin-related toxicity (43).

Polymeric nanoparticles are usually functionalized at their surface with hydrophilic polymers. The chemotherapeutics can be entrapped between the polymeric chains or at the particle's surface to allow the encapsulation and transport of a wide range of therapeutics including drugs, proteins, and nucleic acids. However, the polymeric-based nanoparticles have some disadvantages, such as their weak physicochemical stability that can induce changes in the morphology of the carriers (*i.e.* assembly and disassembly of nanoparticles during storage or blood circulation), which will affect the bioavailability of the loaded compounds. Further, the particle disassembly can also promote a premature release of the loaded cargo, which results in a decrease of the therapeutic effectiveness (36, 42).

Dendrimers are another important class of polymer-based nanoparticles that present a globular nanosized branched structure that can be divided into three domains (44). A core consisting of an atom or molecule, the interior shell formed by branches deriving from the core, and the terminal functional groups (45). These three domains can be tailored to different applications, such as drug or gene delivery (46, 47). The high level of control over the dendrimer architecture, branching length and density, makes it easier to tailor their size, shape, and surface functionality (48). However, they usually present increased immunogenicity and, particularly, the cationic dendrimers have associated a high cytotoxicity, which hinders their application in the clinic (49).

Inorganic nanostructures comprise quantum dots, magnetic nanoparticles, carbon nanotubes, silica nanoparticles and gold nanostructures (35, 36). These different types of inorganic nanocarriers possess unique features to be used as delivery systems, like a robust and stable structure, high loading capacity and a surface easily modified with different components to give them multifunctional capabilities (35). Furthermore, inorganic nanoparticles can exhibit imaging capacities through their magnetic, contrast, and photothermal capabilities (50).

Quantum dots are semiconductor nanocrystals, with a size up to 10 nm. They are mostly applied for bio-imaging, due to their broad absorption and emission peaks in the visible (400 - 700 nm) and near-infrared (NIR) region (700 – 1100 nm) of the spectra (51). However, the hydrophobic surface of quantum dots requires their functionalization with biocompatible materials before they can be used in biological applications. Magnetic nanoparticles such as superparamagnetic iron oxide nanoparticles can serve as contrast agents for imaging purposes. Moreover, these particles also have the capacity to generate heat in response to a magnetic field, allowing their application in magnetic hyperthermia. NanoTherm® is an

example of a commercial available inorganic nanoparticles used for cancer therapy. These nanoparticles demonstrated to be effective in the treatment of glioblastoma (36, 52). Carbon nanotubes are multifunctional platforms that can be used for imaging, drug delivery and thermal ablation of cancer (53). The hydrophobic character of this type of carrier requires their functionalization with hydrophilic molecules to improve their stability and biocompatibility. Although, inorganic nanoparticles have as main drawbacks the absence of biodegradability and the lack of knowledge about their possible long-term toxicity *in vivo* (54).

1.2.2 Nanoparticles benefits for cancer therapy

The utilization of nano-sized carriers has several benefits in comparison to the traditional therapies such as increased drug solubility and stability, protection of drugs from the premature degradation, metabolism and excretion, enhanced blood circulation time and accumulation on the tumor tissues, which ultimately improves the therapeutics outcome (33, 55). Also, due to their reduced size and specific surface properties, nanoparticles can preferentially become accumulated within the tumor tissues (34, 36). This innate accumulation occurs mainly through the enhanced permeability and retention (EPR) effect (Figure 1.5). The EPR effect arises from the defective vasculature present at the tumor tissue (*i.e*. fenestrae with 400 to 600 nm) that allows the nanoparticles to escape from the blood circulation. Moreover, the impaired lymphatic vasculature decreases the nanoparticles removal through the lymphatic drainage, increasing their residence time and accumulation in the tumor (56).

On the other side, nanoparticles can be modified with targeting moieties for exploring ligand-receptor, antigen-antibody and other forms of molecular recognition with molecules overexpressed or uniquely expressed in the constituents of the tumor microenvironment for actively promote their accumulation in the tumor tissues (57, 58). This improved nanoparticle biodistribution can potentiate the therapeutic effect by increasing the drug accumulation within the tumor as well as reducing its interaction with healthy cells (36, 59). Moreover, nanoparticles can also be tailored to release their cargo (*e.g.* drugs, proteins, genetic material, others) in response to specific stimuli present at the tumor site. In fact, in the literature, several nanoparticle-based systems that are responsive to variations in pH, redox environment, temperature, ATP, enzymes or even external triggers such as magnetic field, NIR light, and ultrasounds have been already described (32). When developing stimuli-responsive nanomedicines, the pH is one of the most explored triggers since the tumor environment displays a pH lower than that found in the normal tissues due to the “Warburg effect” (60). The higher cellular proliferation and low blood perfusion (*i.e.* decreased oxygen contents) within the tumor favors the cells’ anaerobic metabolism and consequently increase the production of acid lactic (6, 61). Moreover, a defective lymphatic drainage limits the removal of these acidic waste products. Therefore, in the tumor tissues, nanocarriers find an acidic environment with values ranging from 4.5 to 5.5, which contrasts with the physiological pH 7.4 (62). Therefore nanocarriers have been taking advantage of this pH difference by using materials such as chitosan, poly(acrylic acid), hyaluronic acid, calcium carbonate or even acid-labile chemical linkages (26, 63-65). Other stimuli commonly used as the trigger is the redox environment. In the human body,

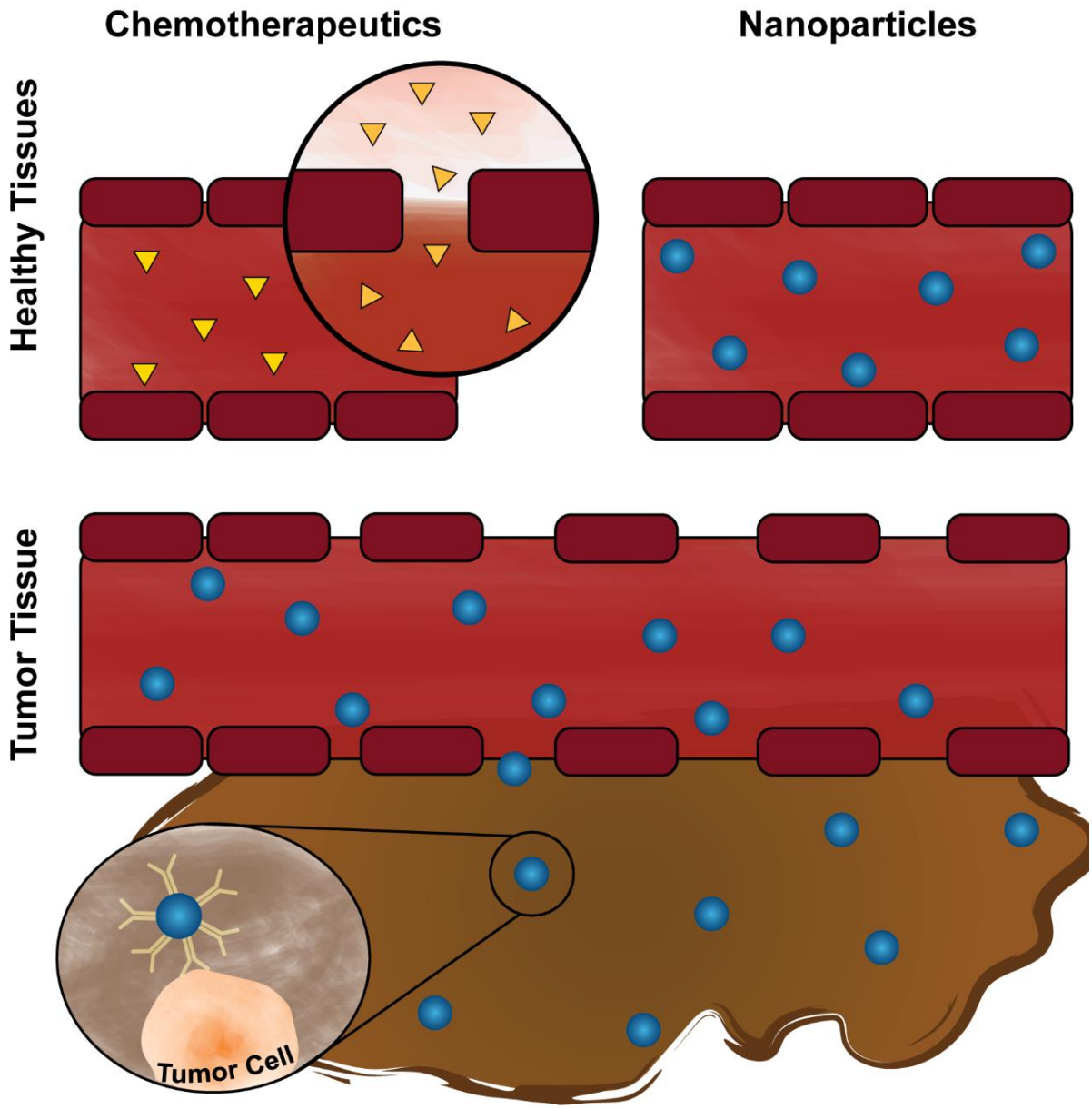

Figure 1.5. Representation of the nanoparticles accumulation in the tumor tissue. The nanoparticles size do not allow the extravasation from the blood vessels into the healthy tissues. However, when nanoparticles reach the tumor region, the defective vasculature favors the nanoparticles accumulation within the tumor, which can be further enhanced by modifying the particles surface with targeting moieties that are specific for some tumor constituents.

the glutathione (GSH)/glutathione disulphide redox couple is the most important scavenger of reactive oxygen species (ROS) protecting cells from exogenous and endogenous toxins (66). The GSH concentration in the tumor cells is 100 to 1000 times higher than in the extracellular fluids, so some nanocarriers explore this stimulus to suffer degradation or disassemble when they reach the cancer cells cytoplasm (67, 68). To accomplish that, redox-responsive nanocarriers have been produced with disulphide bonds (general structure R–S–S–R) that are degraded in the presence of reducing agents, such as GSH (69-71). On the other side, nanocarriers responsive to ATP take advantage of the ATP gradient between the extracellular and intracellular media to promote the release of its cargo (72). The ATP is one of the most important biomolecules in the cells and it is used in the intracellular energy

transfer process. Since the extracellular concentration of ATP is significantly lower than in the cell cytoplasm (0.4 mM *vs* 10 mM), the nanocarriers explore this difference to trigger the cargo release when in the interior of the cell (72). For this purpose, researchers usually explore competitive binding interactions between ATP and the nanocarrier (*e.g.* coatings of ATP aptamers) to promote the cargo release (73, 74). Additionally, external stimuli such as magnetic field, NIR light, and ultrasounds can also be used to prompt the drug release through the nanocarriers thermal or mechanical degradation. In that way, these approaches allow a spatial-temporal controlled release of the therapeutics (Figure 1.6) (75, 76).

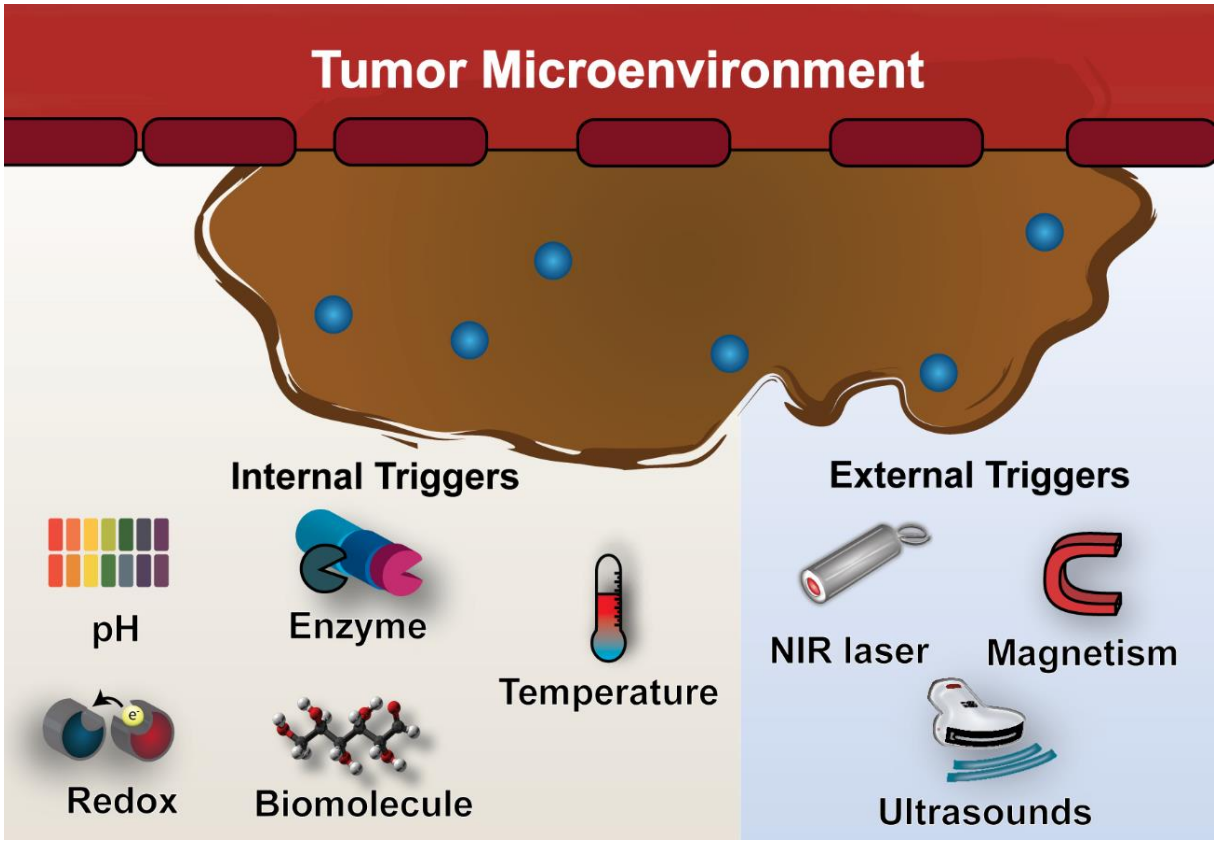

Figure 1.6. Representation of the internal stimuli (pH, enzymes, redox environment, temperature, and biomolecules) or external triggers (NIR laser, magnetism, and ultrasounds) that are used to perform drug release from nanoparticles.

1.2.3 Nanoparticles main properties

Nanocarriers can be administered to the human body through different routes such as oral, nasal, intramuscular and intravenous. Between them, the intravenous administration of nanoparticles is the most used and once nanoparticles are in the bloodstream they must remain stable, avoiding their aggregation and degradation (*e.g.* oxidation and hydrolysis) (77-79). Further, the nanoparticles must evade the rapid clearance by renal filtration and the uptake by reticuloendothelial system (RES) organs, such as liver and spleen, that can capture the nanoparticles and degrade them. On the other side, the nanoparticles should be capable of avoiding the adsorption of plasma proteins (*e.g.* serum albumin, complement compound, and immunoglobulins) to their surface, since it will lead to the nanoparticles

clearance by promoting their recognition by phagocytic cells (Figure 1.7) (80, 81). Additionally, when in the tumor region, nanoparticles should be able to exploit the EPR effect, penetrate through the tumor mass, and reach the cancer cells (36, 82). However, this process can be impaired by the high density of the ECM and the high interstitial fluid pressure found in tumors, leading to a heterogeneous and superficial nanoparticle distribution. In a final step, the nanocarriers should be internalized by cancer cells and release their content in the intracellular compartment (80, 83). These nanoparticle-biological system interactions is dependent on the nanocarriers size, charge, surface composition as well as on its shape (Figure 1.8) (84). These parameters will influence the nanoparticles blood circulation time, retention or removal from the human body, accumulation in the tumor tissue and ultimately the therapeutic outcome (83).

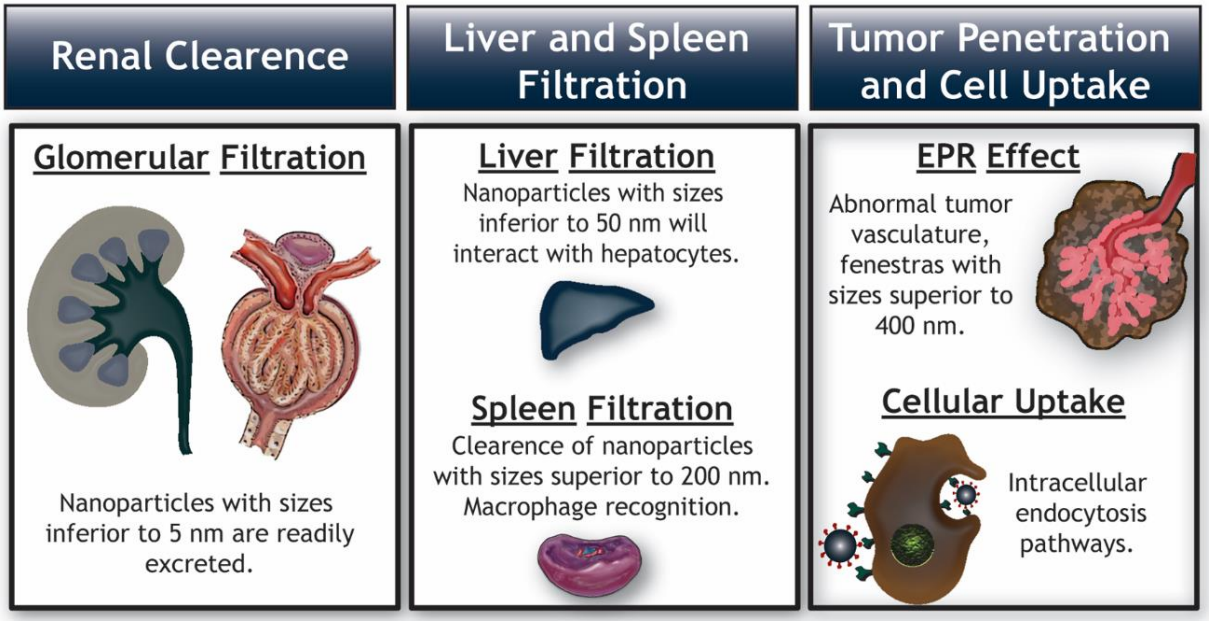

Figure 1.7. Representation of the biological barriers that nanoparticles have to surpass during its circulation in the bloodstream or within the tumor tissue. Nanoparticles must be able to avoid the renal, liver and spleen clearence as well as to extravasate through the tumor vasculature and interact with the target cell. Reproduced from (32).

1.2.4 Nanoparticles size

There are several size limitations that should be considered during the design of the nanoparticles. For example, particles with a size inferior to 5 nm tend to be rapidly eliminated by renal filtration. Additionally, the size also regulates the nanoparticles filtration and uptake by the RES. Nanoparticles with sizes lower than 50 nm can interact with hepatocytes since they can extravasate through the liver fenestrations (50 – 100 nm), while nanoparticles larger than 200 nm are entrapped in the spleen. Moreover, larger nanoparticles can be sequestered by the macrophages residing in the liver and spleen. Therefore, considering these size limitations and those imposed by the EPR effect, the ideal nanoparticle size should be comprehended between 100 and 200 nm (56, 81, 85). Despite the impact on the nanoparticles blood circulation time, the nanoparticles size also influences their tumor penetration. In the literature, larger nanoparticles have shown lower tumor penetration capacity whereas the smaller ones are more prone to penetrate deeper and faster in the tumoral mass (56, 85). Further, smaller nanoparticles (4 –

10 nm) can become internalized in the cancer cells by direct transposition of the lipid bilayer membrane (86). On the other side, bigger nanoparticles can be internalized through pinocytosis in a process comprising clathrin-dependent endocytosis (≈120 nm, destined to lysosomes) or clathrin-independent endocytosis. The later pathway encompasses the caveolin-dependent endocytosis (≈60 nm), clathrin- and caveolin-independent endocytosis (≈120 nm) and macropinocytosis (> 1μm). Therefore, the size affects the fate of the internalized nanoparticles since some uptake routes direct the nanoparticles to the lysosomes, which can lead to the degradation of the loaded cargo by hydrolytic mechanisms (85, 87).

1.2.4.1 Nanoparticles surface composition

The surface components of the nanoparticles play an important role in the nanocarriers biodistribution (56). The nanoparticles surface can be functionalized with hydrophilic polymers, such as PEG, in order to improve their solubility and stability. For example, PEG coatings can also reduce nanoparticles opsonization, protecting them from degradation and reducing their uptake by macrophages (56, 88). However, these properties conferred by the PEG coating are dependent on some factors, such as PEG density and molecular weight. On the other side, some research groups have demonstrated that anti-PEG antibodies can be produced after the injection of the nanocarriers coated with PEG, leading to a rapid elimination of the nanoparticles in subsequent administrations, in a phenomenon termed Accelerated blood clearance (89). In order to avoid this situation, other types of coatings are being investigated, such as the utilization of zwitterionic molecules, polyoxazolines (90) and poly(glycerol) acid (91). Moreover, the nanoparticles surface can also be functionalized with targeting ligands (*e.g.* folic acid and antibodies) to improve their selectivity towards cancer cells (58, 83).

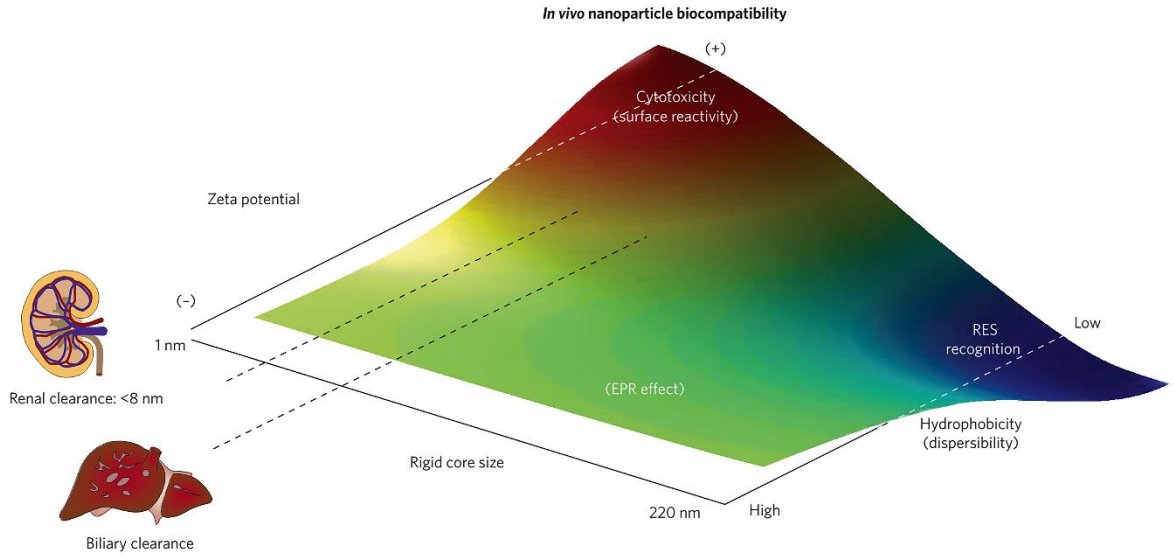

Figure 1.8. Overview of the main properties of nanoparticles that affect their biological performance. The nanoparticles size, charge, surface chemistry, composition, and morphology play an important role in their interaction with the human body. Reproduced from (92).

1.2.4.2 Nanoparticles surface charge

The nanoparticles surface charge is an important parameter that can affect their circulation time in the bloodstream and interaction with cancer cells. Nanoparticles that have a higher surface charge (*i.e.* zeta potential > +10 mV) will interact with blood proteins, leading to their opsonization and clearance, while negatively charged nanoparticles (*i.e.* zeta potential < -10 mV) present an increased uptake by RES. Therefore, a neutral charge (±10 mV) is often referred as ideal for improving nanoparticles blood circulation time, being less prone to suffer opsonization and RES uptake, and consequently favor their accumulation within tumors (56). Additionally, the nanoparticles surface charge can influence their tumor penetration by mediating the nanoparticles interaction with the charged components of the tumor ECM. For example, positively charged particles tend to interact with hyaluronic acid, while the negatively charged ones interact with collagen. Therefore, nanoparticles with a neutral charge have been showing an improved penetration capacity into the tumor tissue (56, 93).

1.2.4.3 Nanoparticles shape

The shape of the nanoparticles is also an important parameter that influences their interaction with the human body. However, the real influence of this parameter on the nanoparticles biological performance has been the subject of debate since the available results are often contradictory. Janát-Amsburyet and co-workers reported that PEGylated gold nanorods have a higher tumor accumulation than gold nanospheres, most likely due to their longer blood circulation time and lower uptake by the liver and spleen (94). On the other hand, Black and co-workers verified that PEGylated gold nanospheres presented a higher tumor accumulation, followed by nanocages, nanodisks, and nanorods. In their study was also verified that nanospheres display a higher blood circulation time and a lower RES organ uptake than nanoparticles with other shapes, leading to their higher accumulation. However, the elongate-shaped materials exhibited a superior tumor residence time. Further, gold nanorods and nanocages had an increased tumor distribution while the nanospheres and nanodisks were mainly confined to the tumor periphery (56, 81, 95). Additionally, the effect of the nanoparticle shape can be material dependent, *i.e.* for nanocarriers produced with silica and iron oxide the non-spherical shape results in an enhanced cellular internalization, while for those made of polymers and gold, the spherical-shape presents an improved cellular uptake (56, 95). Moreover, nanoparticles' shape can also affect their interaction with the macrophages on the bloodstream and consequently their blood circulation time (56, 96). In the literature, worm-like and rod-shaped nanocarriers have shown to be less phagocyted than the spherical-shaped nanoparticles (94, 97).

1.3 Gold nanoparticles properties and their application in cancer therapy

Among the wide variety of nanoparticles reported in the literature, gold nanoparticles assume an increased relevance when biomedical applications are envisioned. Gold is one of the least reactive known metals and presents resistance against oxidation and corrosion (98). Further, gold nanoparticles present unique optical properties, due to the surface plasmon resonance phenomenon (*i.e.* the light scattering or absorption in response to the free electrons synchronized oscillation, when these particles

are exposed to light at their resonance wavelength). The production of gold nanoparticles with different shapes (*e.g.* rods, cubes, triangles, cages, stars or others) has allowed the tuning of the particles' resonance wavelength to the NIR region, a radiation wavelength range where the human body components present almost no absorption (reviewed in detail by (99-102). This control over gold nanoparticles surface plasmon resonance has been exploited to apply them as bioimaging and/or photothermal agents (103-107).

Despite the wide range of applications tested so far for gold nanostructures, these nanoparticles also display some limitations that impair their utilization in biological systems. Gold nanoparticles can interact with compounds containing thiol or disulfide groups through the formation of relatively strong gold-thiolate bonds (108). This well-known gold binding affinity or the establishment of non-specific interactions trigger the adsorption of biomolecules to the nanoparticles' surface (109, 110). Particularly, the adsorption of proteins at nanoparticles surface affect their properties, and thus on their interaction with the human body (*e.g.* nanoparticles uptake, blood circulation time and biocompatibility) (111, 112). Moreover, gold nanoparticles during bioimaging or therapeutic applications can be exposed to high-energy laser pulses and a portion of the incident radiation is converted into heat (113). In turn, the generated heat can lead to the gold nanoparticle reshaping (*i.e*. melting) and, consequently, to the loss of their optical properties (100, 114). Therefore, the post-synthesis modification of gold nanoparticles is highly desirable for surpassing these limitations as well as to potentiate gold-based nanoparticles application in nanomedicine (115-117). From the wide number of materials used in the literature (*e.g.* dextran, poly(isobutylene-alt-maleic anhydride)-graft-dodecyl and PEG), silica arises as one of the main coating alternatives for gold nanoparticles (118, 119).

1.3.1 Gold core silica-shell nanoparticles

Nanoparticles produced with silica have been reported as stable colloidal suspensions, chemically inert, biocompatible and that can be modified with different functional groups (120, 121). Further, silica derivatives such as mesoporous silica possess a large surface area and pores that can act as reservoirs for bioactive molecules aimed for therapeutic purposes (30, 120). Such features allow the encapsulation of poorly soluble compounds, conferring them protection from premature degradation and clearance from the human body (122, 123). In addition, the inclusion of the silica shell also enhances the colloidal stability of gold nanoparticles when they are in contact with biological fluids or irradiated with a specific radiation (124, 125). Silica is also optically transparent to the NIR radiation, often used in photothermal therapy (PTT), which is fundamental to not compromise the therapeutic capacity of gold-based PTT agents (126, 127). Therefore, the multifunctional potential of gold core-silica shell (AuMSS) nanoparticles provides an ideal platform for theragnostic modalities combining therapeutic, targeting, and imaging functions (please see Figure 1.9).

During the past years, a huge effort has been done to allow the fabrication of AuMSS nanoparticles in a scalable, controlled and reproducible manner (128-130). Generally, the production of these nanoparticles can be achieved through two main steps (please see Figure 1.10): i) the production of the gold core with the desired size and shape and ii) the synthesis of the silica shell (128, 131, 132). The gold cores can be synthesized using different synthetic routes to yield gold nanoparticles with distinct

sizes and shapes, as extensively reviewed in (101, 133-135). Briefly, gold cores are usually prepared by inducing the reduction of gold salts and consequent gold nucleation and growth in the presence of a stabilizing agent, such as trisodium citrate and cetyltrimethylammonium bromide (CTAB), to prevent the particles to become aggregated (135).

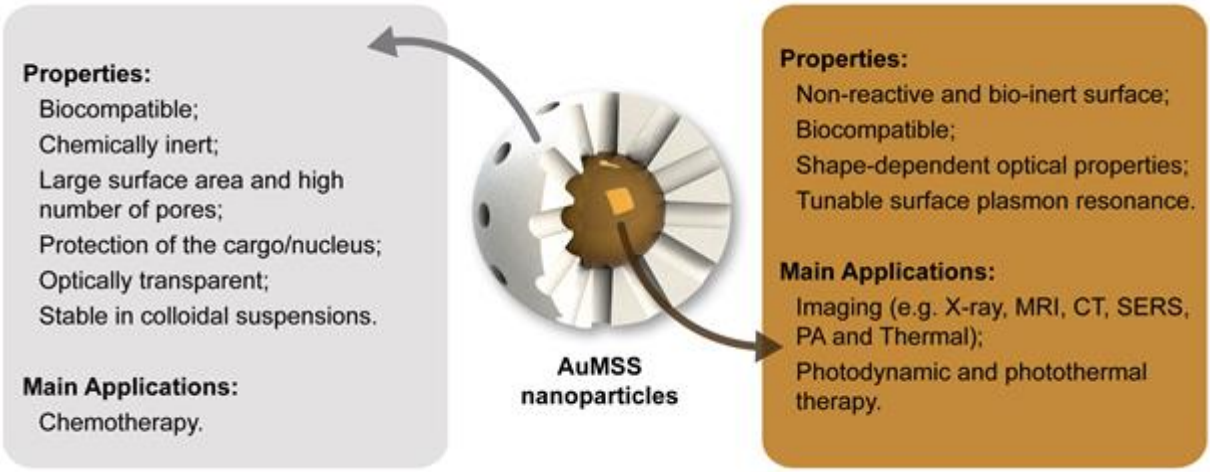

Figure 1.9. General properties and main applications of the AuMSS nanoparticles. The gold core allows the particle application in bioimaging and PTT. The inclusion of the silica shell stabilizes the gold core and improves drug delivery capacity of the nanoparticles.

Nanoparticles with spherical shape are the most stable and can be obtained when the gold core synthesis is performed under thermodynamically controlled conditions (136). Alternatively, to obtain nonspherical gold-cores the synthesis process must be fine-tuned to favor an anisotropic growth of the gold core by using surfactants that block some of the growing directions (*e.g.* CTAB (137, 138), halides (139, 140) or weak/mild reduction agents (141, 142)). Up to date, the rod-like shape remains as one of the most explored gold nanostructures. In general, gold nanorods are produced by using a seed-mediated growth methodology (132, 143), where small spherical gold spheres (*i.e.* seeds) are synthesized by nucleation and then they are added to a solution denominated of "growth solution", which is composed of a gold salt (*e.g.* chloroauric acid), silver nitrate and high concentrations of CTAB to induce the rod-shaped growth (143). Gold nanostars and nanocages have also been used for biomedical applications. Gold nanostars are also produced by using a seed-mediated growth method. However, the particle growth occurs in the surface of poly(vinyl pyrrolidone) coated gold seeds in the presence of dimethylformamide (144). On the other hand, gold nanocages are prepared by using sacrificial silver nanocubes which are exchanged by gold through a galvanic replacement process (145). Subsequently, the silica coating of the gold cores is accomplished by using the classic Stöber method or its derivations (130, 146). During the synthesis procedure, the silica precursor (*e.g.* tetraethyl orthosilicate (TEOS)) molecules will start to condensate around the gold core originating the silica shell. The thickness of this silica shell can be tailored by fine-tuning the reaction time and reagent concentrations (146). In these systems, the optical and electronic properties can be adjusted by varying the shape and size of the gold core as well as the thickness of the silica shell (147, 148). On the other side, the silica coating allows the stabilization of the gold nanostructures as well as the encapsulation of drugs, dye molecules, or

other imaging agents (32, 149). Further, silica presents an increased surface area that can be functionalized with antibodies, targeting moieties or even stealth agents (32, 122). Therefore, AuMSS nanoparticles with different core shapes (*i.e.* spheres, rods, stars, and cages) have been employed for therapeutic and bioimaging applications (150-152). AuMSS nanoparticles have been explored to mediate single or combinatorial therapeutic approaches based on drug delivery, PTT and photodynamic therapy (PDT) (107, 153-156). The possibility to combine different therapeutic functions into one nanoparticle is benefic, since it improves the therapeutic efficacy, due to possible synergic interactions, and minimizes the side-effects originated by the administration of multiple doses (33, 157). Further, the gold-core allows its use in bioimaging techniques such as computerized tomography (CT), magnetic resonance imaging (MRI), photoacoustic (PA) imaging and surface enhanced Raman spectroscopy (SERS) (158, 159).

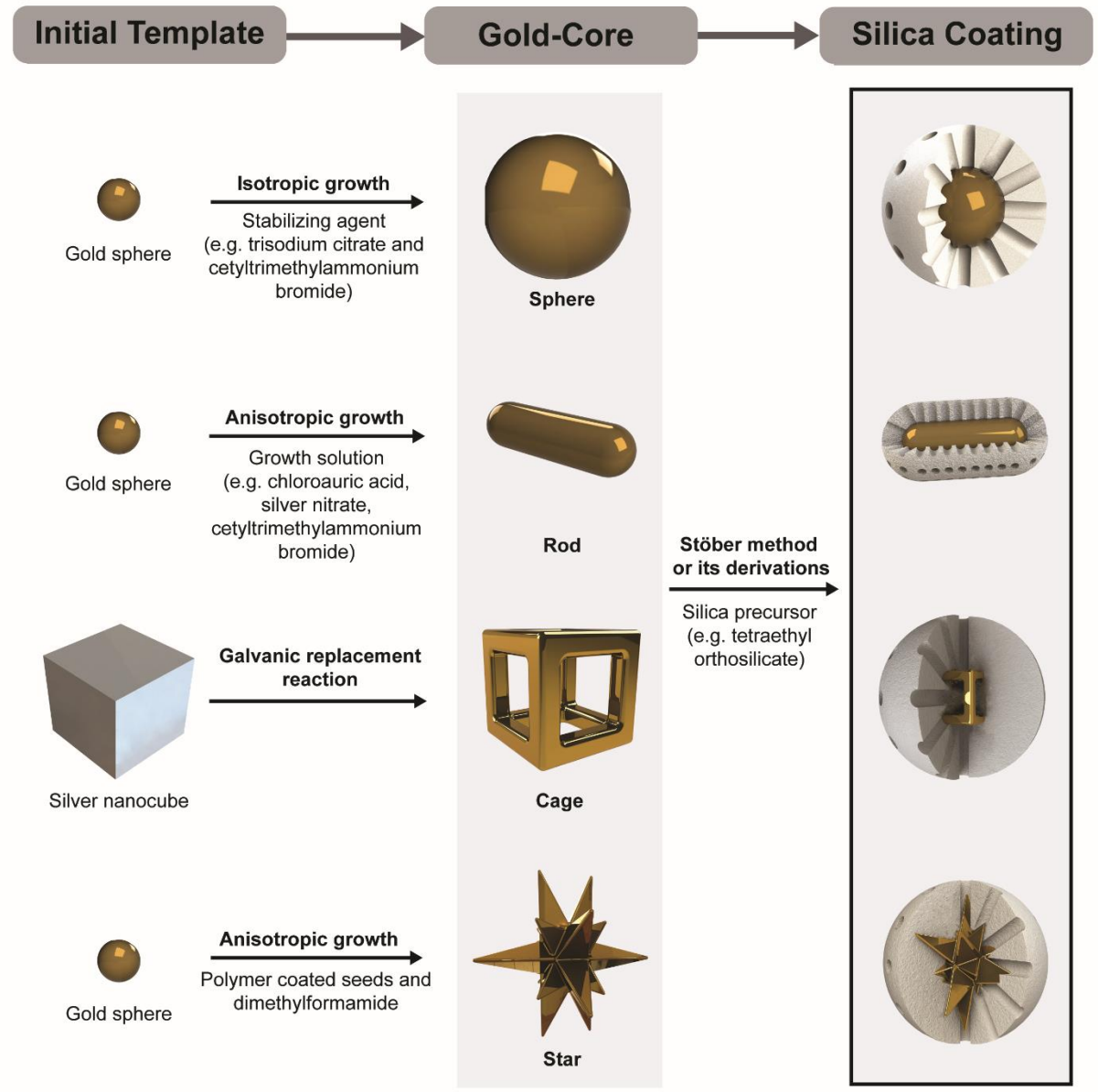

Figure 1.10. Representation of AuMSS production processes. The production of the gold-core can be achieved by promoting an isotropic or anisotropic growth as well as through sacrificial templates. Afterwards, the gold-core with the desired shape is coated with a silica layer by using the Stöber method or its derivations.

1.3.1.1 AuMSS nanoparticles biocompatibility

The application of AuMSS nanoparticles in the clinic is dependent on the complete understanding of the nanoparticles-host interactions that occur upon administration. Therefore, several extensive *in vitro* and *in vivo* toxicological studies are currently being performed (160-162). Zeng and colleagues reported that the cytotoxicity of AuMSS nanospheres is size and dose-dependent (162). The AuMSS nanospheres with 50, 100 and 200 nm silica layers did not induce any significant cytotoxicity in concentrations inferior to 200 pmol/L, whereas when the concentration was increased to 400 pmol/L, the spheres with 200 nm silica layer decreased the liver hepatocellular carcinoma (HepG2) cell viability in 10%. In another work, Dias and colleagues compared the cytotoxicity of spherical and rod-like AuMSS nanoparticles (75). The administration of both spherical and rod-like nanoparticles to Human negroid cervix epithelioid carcinoma (HeLa) cells and human fibroblasts revealed that both systems were biocompatible up to 100 µg/mL. Moreover, the authors observed that the rod-like shaped nanoparticles exerted a positive effect on the cell migration capacity, presenting a gap with a smaller width than the cells treated with the spherical AuMSS in the *in vitro* wound closure assays. Apart from the acute toxicity of the AuMSS nanoparticles, the systemic toxicity and distribution greatly impact on the biological performance of these nanoparticles. Thakor *et al.* studied the systemic biodistribution and acute effects of PEGylated AuMSS nanospheres (size 120 nm) administered intravenously in mice (161). Their initial results demonstrated that the particles did not affect the physical appearance, behavior or social interactions of any mice used in the study, neither induce any acute effects on basal cardiovascular function and on hematological and biochemical parameters recorded. Furthermore, the authors observed that the PEGylated AuMSS nanospheres were mainly accumulated in the liver and spleen, inducing a mild inflammatory response in the liver through ROS formation at 24 h post administration, but the nanoparticles were not detected 1 week after injection. In turn, Gao *et al.* evaluated the biocompatibility and biodistribution of folic acid functionalized AuMSS nanorods in rabbits (160). In their study, particles concentration up to 40 ppm did not elicit any significant cytotoxic effect on HepG2 cells. Further, the folic acid functionalized AuMSS displayed a preferential accumulation in the tumor tissues and started to be cleared from the body after 24 h, through renal filtration. Moreover, no serious signs of toxicity in vital organs were noticed by the authors even when higher doses (10.5 mg/kg) were administered. Despite, to rationally apply AuMSS nanoparticles in the clinic, it is still necessary to perform additional studies, such as the characterization of the AuMSS particle shape and administration route influence on the particles performance, to better understand the AuMSS particles behavior in biological environments.

1.3.1.2 Rod-like AuMSS nanoparticles

The rod-like shaped nanoparticles are the most explored AuMSS particles when therapeutic applications are intended. The increasing interest triggered by AuMSS nanorods is based on their tunable optical properties and effective light-heat conversion (102, 111). The AuMSS nanorods present two distinct absorption peaks that correspond to the transverse and longitudinal resonances (102). The transverse resonance leads to an absorption peak at 520 nm, whereas the longitudinal resonance can be easily tuned to present a higher absorption within the NIR region, through the manipulation of the rod aspect

ratio (AR), *i.e.* rod length/width coefficient (163). These important characteristics favor the AuMSS nanorods application in imaging (PA and X-ray) and therapy (*e.g.* chemotherapy, PTT, PDT or their combination) (164-166). The PA imaging takes advantage of the ultrasounds generated by the temperature increase and the rapid pressure differences created by NIR laser irradiation of AuMSS nanorods (159). Cheng *et al.* demonstrated that AuMSS nanorods present an increased stability when compared to bare and PEGylated gold nanorods, for being applied in PA imaging (113). The extra protection provided by the silica shell (*i.e*. thickness 6 nm or 20 nm) resulted in the stabilization of the PA signal during 300 pulses. In contrast, the signal of PEGylated gold nanorods decreased 40% in the first 100 pulses. Further, these researchers also reported that the inclusion of the 20 nm silica shell increases the amplitude of the PA signal generated by the gold nanorods, which can lead to clear and better images (113). Apart from imaging, the AuMSS nanorods capacity to absorb radiation in the NIR region have also been explored to mediate therapeutic applications, mainly in cancer PTT therapy (167, 168). Liu *et al.* developed a tLyp-1 peptide-functionalized, indocyanine green-loaded AuMSS nanorods for the breast cancer PTT treatment and indocyanine green-mediated imaging (169). The nanorods had an AR of 3.5 (length 47 nm and width 14 nm) with a 17–32 nm silica shell and presented a strong absorption peak in the NIR region, at 754 nm. Further, the nanoparticles mediated an increase in the temperature up to 55 °C and a decrease in MDA-MB-231 cells viability to values as lower as 20%, when irradiated with a NIR laser (785 nm, 3 $W.cm^{-2}$ for 2 min). Similarly, Lee *et al.* developed an RVG29 (29 residue peptide derived from rabies virus glycoprotein) functionalized AuMSS nanorods to be used in the PTT treatment of brain gliomas (170). The produced AuMSS nanorods had an AR of 2.4 (length 180 nm, width 75 nm, and 14 nm shell thickness) and presented an higher absorption in the NIR region. The RVG29 functionalization of the AuMSS nanorods proved to be capable of increasing the nanoparticles accumulation in the brain region of glioma-bearing mice. Further, the nanoparticles NIR laser irradiation (808 nm, 5 min, and 1.5 $W.cm^{-2}$) increased the temperature of the tumor site to values around the 50 °C, thus supressing the growth of the xenografted tumor and allowed the real-time monitoring via MRI, along the study (170). However, the AuMSS-mediated PTT therapy is hindered by light scattering and absorption phenomena that occur when the NIR light travels deeper into the tissues (171, 172). Therefore, depending on tumor location, some cells will inevitably receive suboptimal laser exposure and survive (171, 172). With that in mind, several studies have been combining the AuMSS-mediated PTT with chemotherapy or PDT to improve the therapeutic outcome (154, 173). Shen and colleagues produced doxorubicin loaded AuMSS nanorods functionalized with arginyl-glycyl-aspartic acid (RGD) sequence for the targeted chemo- and PTT combinatorial therapy (174). The particles presented a AR 3.9 (length 52 nm, width 13 nm, and 25 nm shell thickness), strong absorption in the NIR wavelength region (absorption peak at 840 nm) and a drug release that could be induced by the NIR laser irradiation and consequent heat generation. Additionally, the nanoparticles intravenous administration in A549 tumor bearing mice revealed that the nanoparticles could mediate an increase in the tumor temperature up to 65.9 °C, after NIR laser irradiation (808 nm, 30 s, and 3 $W.cm^{-2}$). In addition, the anti-tumoral effect of the nanorods was enhanced when chemo and thermal therapies were combined, being registered a tumor weight inhibition rate of 66.5% and 45.2% for the combinatorial therapy and single PTT therapy, respectively. Recently, Zhou *et al.* developed hyaluronic acid and RGD peptide functionalized AuMSS

nanorods loaded with doxorubicin for the combinatorial therapy of ovarian cancer. The nanorods (length 50 nm, width 10 nm, and shell thickness of 15 nm) irradiation with NIR laser (808 nm, 2 $W.cm^{-2}$ and 4 min) resulted in an improved therapeutic effect towards ovarian SKOV-3 cancer cells (10%, 29% and 46.5% cell viability for combinatorial, chemotherapy and PTT, respectively) (168). With a different approach, Moreira and colleagues encapsulated AuMSS nanorods loaded with doxorubicin within poly (lactic-co-glycolic acid) based microparticles containing salicylic acid for the chemotherapy and PTT combinatorial therapy of cervical cancer (76). The authors observed that the heat generated by the nanorods irradiation with a NIR laser (808 nm, 1.7 $W.cm^{-2}$ and 5 min) could trigger the drug release and enhance the particles cytotoxicity, *i.e.* the cell viability within HeLa spheroids was reduced to 25%, when spheroids were irradiated with NIR laser, whereas in the non-irradiated group 50% of the cells remained viable. On the other side, Seo *et al.* explored the combination of the PTT and PDT by using AuMSS nanorods (length 32 nm, width 11 nm, and shell thickness 20 nm) loaded with methylene blue (175). Upon NIR laser irradiation (780 nm, 1 $W.cm^{-2}$), the authors reported a synergistic effect between the heat generated by the nanorods and the ROS created by the irradiation of the methylene blue molecules leading to a decrease in the cell viability up to 11%. Moreover, these nanoparticles also allowed the detection of both agglomerated and single cancer cells through SERS imaging. In an integrative study, Luo and colleagues developed cisplatin and Al(III) phthalocyanine chloride tetrasulfonic acid loaded AuMSS nanorods functionalized with β-cyclodextrins, adamantine conjugated PEG and lactobionic acid in order to be applied in PTT, PDT, and chemotherapy of hepatic cancer(176). The intravenous administration of AuMSS nanorods (length 40 nm, width 10 nm, and shell thickness 14 nm) triple therapy in HepG2 tumor-bearing mice increased the temperature at the tumor site to 53 °C and ceased the tumor progression upon irradiation with NIR laser (808 nm and 606 nm, 1 $W.cm^{-2}$ for 5 min). In sharp contrast, the tumor continued to progress when only PTT/chemotherapy (4-fold volume increase) or PDT/chemotherapy (4.9-fold volume increase) were used.

1.3.1.3 Cage-like AuMSS nanoparticles

Gold-based nanocages have a hollow structure with porous walls and are usually synthesized through a galvanic replacement reaction between silver nanocube templates and the gold precursor (177, 178). In these structures, the surface plasmon resonance peak can be adjusted to the NIR region of the spectra by fine-tuning the amount of gold precursor (179). Additionally, the silica coating thickness can also influence the plasmon resonance peak. Khlebtsov and colleagues observed that an increase in the thickness of the silica shell (12–127 nm) result in a shift of the plasmon resonance peak to higher wavelengths, from 775 nm to 817 nm (180). Additionally, the structural organization of AuMSS nanocages allows the drug encapsulation both in the hollow space of the gold nanocage as well as in the outer mesopores of the silica shell (156, 181). Khlebtsov *et al.* explored the application of Yb-2,4-dimethoxyhematoporphyrin loaded AuMSS nanocages for the PDT and PTT of cervical cancer (182). The nanocages presented an average size of 140 nm with a shell thickness of 45 nm and a pronounced absorption peak in the NIR region, at 790 nm. Moreover, these nanocages were able to increase the temperature up to 75 °C, after being irradiated for 5 min (808 nm and 1 $W.cm^{-2}$). Additionally, the irradiation of the particles with a 625 nm laser (50 $mW.cm^{-2}$ and 15 min) resulted in the reduction of the

HeLa cells viability to 25%, via a PDT mediated effect. In a different study, Khlebtsov and colleagues also demonstrated that these Yb,4-dimethoxyhematoporphyrin loaded AuMSS nanocages are able to reduce the bacteria cell viability through PTT and PTD approaches (183). On the other hand, Yang and colleagues produced poly(Nisopropylacrylamide) (PNIPAM) coated AuMSS nanocages to attain a stimuli-responsive doxorubicin release towards cervical cancer cells (156). When irradiated with NIR laser (808 nm, 1 $W.cm^{-2,}$ and 10 min) these nanoparticles (size 126 nm and 33 nm shell thickness) mediated an increase in the temperature from 25 °C to 41 °C, which prompted the drug release due to the conformational changes in PNIPAM. Besides, the heat generated also contributed for the improvement of the therapeutic efficiency, *i.e.* HeLa cell viability was reduced to 85.5%, 80.6% and 19.9% when chemotherapy, PTT, and chemo-PTT combination were used, respectively. Hu *et al.* verified the application of Tat peptide-capped AuMSS nanocages loaded with doxorubicin in SERS imaging and chemo-PTT therapy (184). The nanocages (size 129 nm and 45 nm shell thickness) administration to breast cancer cells in conjugation with NIR laser irradiation (808 nm and 123.8 $mW.cm^{-2}$) decreased the cell viability to 21.1% and, simultaneously, allowed the real-time imaging of the MCF-7 cells.

1.3.1.4 Star-shaped AuMSS nanoparticles

The gold nanostar cores are highly anisotropic nanoparticles composed of a small spherical core and a variable number of tips (155). The optical properties displayed by these nanoparticles are strongly related to the size and number of tips and, usually, present a high absorption in the NIR region due to the nucleus and tips plasmons hybridization interactions (185). Atta and colleagues observed that the growth of the silica shell from 12.2 nm up to 29 nm modify the UV–vis spectra of the aminothiophenol doped nanostars (186). The increase in the silica shell thickness promotes an increase in the intensity of the absorption peak and amplifies the obtained SERS signal (186). In turn, Harmsem *et al.* demonstrated the applicability of the PEGylated AuMSS nanostars (size 75 nm) doped with IR-780 in the SERS based imaging of breast cancer, sarcoma, pancreatic ductal adenocarcinoma, and prostate cancer in mice (187). These authors reported that the high sensitivity and signal specificity of the IR-780 doped AuMSS nanostars allowed the detection of primary tumors as well as premalignant lesions smaller than 100 μm. In addition, these nanostars also identified small malignant cell remains that would lead to the cancer recurrence, even after the authors performed the resection. On the other hand, Fales *et al.* reported the application of methylene blue loaded AuMSS nanostars doped with 3,30-diethylthiatricarbocyanine iodide for simultaneous SERS imaging and PDT of breast cancer (188). The authors observed that the nanostars irradiation (785 nm, 300 $mW.cm^{-2}$, for 10 s) resulted in a strong SERS signal, whereas the irradiation at 633 nm, 900 $mW.cm^{-2}$, for 1 h, prompted the ROS production. This particle behavior led to the death of BT549 breast cancer cells within the spot irradiated with the laser. In another study, Li and colleagues produced PEGylated gold-silica shell nanostars loaded with perflurohexane for multimodal imaging and PTT of glioma xenograft models (189). When irradiated with NIR laser (808 nm, 1.2$W.cm^{-2}$ for 10 min), the nanostars mediated an increase in the tumor temperature to 70 °C resulting in an apoptosis rate of 84% and allowed the tumors imaging via ultrasounds, CT, PA, and thermography. An *et al.* evaluated the application of folic acid-PEG-phospholipid coated AuMSS

nanostars loaded with doxorubicin in the cervical cancer therapy and imaging (190). The authors observed that the nanostars (size 50 nm and 60 nm shell thickness) allowed both PA and CT imaging of the tumors, increased the temperature to 65 °C at the tumor site under NIR laser irradiation and presented a heat-responsive drug release profile. Further, the conjugation of the chemo and PTT therapies induced the tumor necrosis and eradication, being observed only one relapse in the five mice tested at day 12. In contrast, doxorubicin and PTT stand-alone treatments presented a low efficacy, being only capable of reducing the tumor growth rate or inhibit the tumor growth until day 8, respectively.

1.3.1.5 Spherical nanoparticles

The majority of the nanoparticles produced up to now present a spherical shape. The size and relatively simple synthesis of spherical AuMSS nanoparticles make them appealing for applications in the clinic (75). Up to now, these spherical AuMSS nanoparticles have been mainly applied as imaging agents (152, 158). The gold core has the capacity to improve the image contrast in structural imaging modalities, such as CT and MRI. In fact, the mass attenuation of gold, at energies superior to 80 kV, is higher than that of the iodinated contrast agents usually applied in the clinic, which can result in images with a superior resolution (191-193). Kobayashi and colleagues prepared a colloidal solution of AuMSS nanoparticles with a gold nucleus of 17 nm of diameter and total particle size of 136 nm to be used as a CT contrast agent (194). In their work, the authors showed that the AuMSS nanoparticles attenuation capacity was almost seven times higher than Iopamiron®, a commercial iodine based X-ray contrast agent. Further, the contrast of different mice tissues (*e.g.* liver, spleen, and kidneys) was also monitored along time. The authors noticed that the liver and spleen contrast increased (76.7 and 96.5 HU to 115.0 and 120.2 HU, respectively) 5 min after the particles are injected and remained constant for 2 days allowing the obtainment of clear images of the liver and spleen throughout the study (194). Schooneveld *et al.* also developed spherical AuMSS nanoparticles with 88 nm size (*i.e.* gold core with 66 nm coated with an 11 nm silica shell), further modified with paramagnetic gadolinium diethylene triamine pentaaceticacid di (stearylamide), fluorescent Cyanine5.5 conjugated 1,2-distearoyl-sn-glycero-3-phosphoethanolamine(DSPE)-N-mPEG-2000 and PEG-DSPE amphiphiles to be used as contrast agents in different techniques such as MRI, CT, fluorescence imaging and positron emission tomography (195). The addition of this PEGylated lipid layer to the surface of the AuMSS nanoparticles improved the long-term stability of the nanoparticles (*i.e.* particles were stable in aqueous suspension for at least 3 months). Further, the *in vitro* studies performed in J774A.1 macrophage cells revealed that it was possible to monitor the nanoparticles cellular internalization by using MRI, CT, and confocal microscopy. Moreover, when intravenously administered in wild-type C57Bl mice the nanoparticles enhanced the CT and MRI signals (by 50% and 24%), respectively, even when particle doses in the nanomolar ranges (0.15 nmol kg^{-1}) were used (195). In a similar approach, Kircher and colleagues produced a 60 nm gold core covered with trans-1,2-bis(4-pyridyl)-ethylene, a raman molecular tag, and a 30 nm silica layer further functionalized with 1,4,7,10-tetraazacyclododecane-1,4,7,10-tetraacetic acid (DOTA)-Gd^{3+} that allowed the detection and imaging of glioblastoma cells through MRI, CT, and SERS imaging on glioblastoma bearing mice (196). Further, 30 min after the intravenous injection, the authors observed that the nanoparticles increased the MRI image contrast to noise ratio from 1.4 to 8.7 and the

PA signal in 60%, remaining these values stable for 24 h (196). Another prominent application of spherical AuMSS nanoparticles is therapy. The mesoporous silica coating provides pores that can act as reservoirs for the encapsulation of therapeutic molecules in a more efficient way than bare gold nanospheres (32). In our group, Dias and colleagues demonstrated that doxorubicin can be loaded onto the mesopores of the silica shell and delivered successfully to cancer cells (75). The *in vitro* studies performed in 2D and 3D cell cultures showed that these spherical nanoparticles with a size of 109 nm (20 nm gold core and 45 nm silica shell) were efficiently uptaken by cancer cells and could penetrate into deeper regions of spheroids of HeLa cancer cells. Further, after 48 h of incubation, the doxorubicin loaded AuMSS nanoparticles were able to reduce the cancer cells viability to 20% when a 100 μg/mL dose was used (75). On the other side, Ramasamy used AuMSS nanoparticles loaded with cinnamaldehyde, an antimicrobial compound, for the treatment of bacterial biofilms (197). During the nanoparticles production, cinnamaldehyde was chemically linked to gold nanoparticles through an imine linkage and covered with the silica shell, which stabilizes and protects the cinnamaldehyde from premature degradation, leading to a final particle size of 326 nm. The antibiofilm capacity of this nanosystem was then evaluated using different pathogenic strains, such as *Escherichia coli*, *Pseudomona aeruginosa*, methicillin-sensitive *Staphylococcus aureus,* and methicillin-resistant *Staphylococcus aureus*. The authors observed through confocal microscopy and by optical density measurements that the nanoparticles were able to potentiate the antimicrobial activity of cinnamaldehyde effect, by inhibiting the biofilm formation for each of the four bacteria strains (197). Nevertheless, the use of spherical AuMSS nanoparticles in PTT and PDT therapeutic based applications is hindered by their absorbance peak, which is localized in the visible region of the spectra, at around 520 nm (172). Therefore, different particle shapes (rod, stars, and cages) presenting an absorbance peak in the NIR region (*i.e.* so-called “biological window”) have been gaining an increased relevance when therapeutic applications are aimed.

During the last years, the uncontrolled drug release profile, limited blood circulation, and unfavorable pharmacokinetics are the main factors that have limited the AuMSS application in the clinic. Therefore, the practical research developed in this field has been focused on the development of novel AuMSS coatings capable of improving the nanoparticles circulation time and control over the drug release. These characteristics will improve the nanoparticles probability to accumulate within the tumor tissue, while simultaneously decrease the chemotherapeutics interaction with healthy tissues, which ultimately enhance the therapeutic effect.

1.4. Aims

The main goal of this MSc work plan was to design and develop a novel AuMSS surface modification strategy based on the post-synthesis chemical grafting of biofunctional polymers to surpass the nanoparticles uncontrolled drug release and limited blood circulation. For that purpose, the coating of spherical shaped AuMSS nanoparticles with poly-2-ethyl-2-oxazoline (PEOZ) and β-cyclodextrin (β-CD) was optimized.

Therefore, the specific objectives include:

- → Synthesis, purification, and characterization of AuMSS nanospheres;
- → Synthesis of TESPIC-PEOZ and TESPIC- β-CD polymers;
- → Functionalization of AuMSS and characterization of the nanocarriers' physicochemical properties;
- → Characterization of the AuMSS formulations cytocompatibility;
- → Evaluation of the AuMSS uptake in Hela cells.

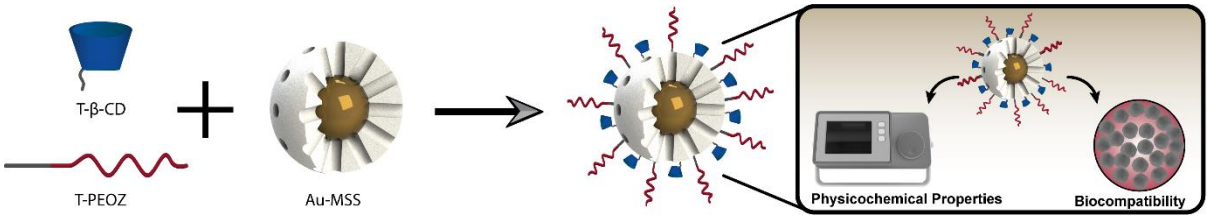

Figure 1.11. Schematics of the main objectives and pratical approach explored for the development of PEOZ and β-CD coated AuMSS nanospheres.

Chapter 2

Materials and Methods

2. Materials and Methods

2.1. Materials

Hydrogen tetrachloroaurate (III) hydrate (HAuCl4) was purchased from Alfa Aesar (Karlsruhe, Germany). Tetraethylorthosilicate (TEOS) and tetrahydrofuran (THF) were bought to Acros Organics (Geel, Belgium). Hexadecyltrimethylammonium bromide (CTAB) and β-CD (Mw: 1135 g/mol) were obtained from Tokyo Chemical Industry Europe (Zwijndrecht, Belgium). Hydrochloric acid (HCl) was acquired from Panreac (Barcelona, Spain). Methanol was obtained from VWR International (Carnaxide, Portugal). 3-(Triethoxysilyl)propyl isocyanate (TESPIC), Dulbecco's Modified Eagle medium-high glucose (DMEM-HG), resazurin, phosphate-buffered saline solution (PBS), ethanol (EtOH), formaldehyde, trypsin, resazurin, Triton-X, ethylenediamine tetraacetic acid (EDTA) and fluorescein isothiocyanate (FITC) were purchased from Sigma-Aldrich (Sintra, Portugal). PEOZ (Mw: 5000 g/mol) was obtained from Polysciences (Bergstrasse, Germany). Fetal bovine serum (FBS) was bought to Biochrom AG (Berlin, Germany). Hoechst 33342® and wheat germ agglutinin conjugate Alexa 594® (WGA-Alexa Fluor® 594) were purchased from Invitrogen (Carlsbad, CA). Cell culture t-flasks were obtained from Orange Scientific (Braine-l'Alleud, Belgium). Cell imaging plates were acquired from Ibidi GmbH (Munich, Germany).

2.2. Methods

2.2.1. Synthesis of AuMSS nanospheres

AuMSS nanospheres were synthesized by adapting a method previously described in the literature (75). In the first step, a small spherical gold core is produced by adding, under stirring at 80 °C, 1 mL of formaldehyde (3.7 wt%) and 0.800 mL of HAuCl4 (0.05 M) to 24 mL of ultrapure water (resistivity 18 mΩ) containing 0.05 g of CTAB and NaOH (0.5 M). After 10 min, 0.897 mL of TEOS (33% v/v in methanol) were added to the previous solution and left to react for 1 h under vigorous stirring and reflux conditions, originating the mesoporous silica shell. The produced gold-core mesoporous silica shell nanospheres were then recovered by centrifugation at 11000g and 25 °C.

2.2.2. Removal of the surfactant template

The extraction of the cytotoxic CTAB template from the AuMSS nanospheres was performed by adapting a solvent based approach described in the literature (76). Briefly, several washing steps were performed by resuspending the AuMSS nanospheres in an acidic solution (HCl 10% v/v in ethanol) and sonicating them for 1 min. After, the nanoparticles were washed several times with absolute ethanol at 4 °C, in order to allow the complete removal of the CTAB and HCl residues. Finally, the particles were resuspended in ultrapure water, recovered by centrifugation (18000g for 15 min) and freeze-dried.

2.2.3. Poly-2-ethyl-oxazoline and β-cyclodextrin modification

PEOZs and β-CDs silane derivatives were produced through a hydrogen-transfer nucleophilic addition reaction between the polymers hydroxyl groups and isocyanate groups of TESPIC. The addition of TESPIC to the polymers chain will allow their chemical coupling to the AuMSS surface (198). For that purpose, PEOZs or β-CDs were dissolved in 30 mL of dry THF and left at 70 °C under a nitrogen atmosphere and vigorous stirring. After 6 h, TESPIC was added to the reaction (molar ratio of 1:1) and left for 24 h under vigorous stirring. At the end of the reaction, the product was recovered by evaporation and centrifugation at 8000g and 4 °C. The successful production of the polymer silane derivatives was assessed by using Fourier transform infrared (FTIR) spectroscopy.

2.2.4. AuMSS functionalization

The surface of AuMSS nanospheres was functionalized by adapting a method previously described in the literature (199). Briefly, the AuMSS nanospheres were resuspended in toluene and left under stirring for 15 min, at 90 °C. Then PEOZ and β-CD at different mass ratios (25/75, 50/50 and 75/25) were added to the solution and stirred for 24 h. The polymer functionalized AuMSS (AuMSS+Polymer 25/75, AuMSS+Polymer 50/50 and AuMSS+Polymer 75/25) nanospheres were recovered by centrifugation at 11000g and 25 °C. The particles were them washed with water to remove unlinked polymer chains.

2.2.5. Characterization of nanocarriers' physicochemical properties

2.2.5.1. Morphological characterization

The morphology of both coated and uncoated AuMSS rods was characterized by Transmission Electron Microscopy (TEM – Hitachi-HT7700, Japan). The nanoparticles samples were placed on formvar-coated copper grids and allowed to dry at room temperature. The images were acquired at an accelerating voltage of 80 kV. After image acquisition, the silica shell thickness and core size were measured by using a specific software (Image J 2.0.0, NIH Image, USA).

2.2.5.2. Size and zeta potential analysis

The size and zeta potential measurement of coated and uncoated AuMSS nanospheres was performed by using a Zetasizer Nano ZS equipment (Malvern Instruments, Worcestershire, UK). In all the measurements, the nanoparticles were previously resuspended in ultrapure water, and the data was collected at 25 ºC in a disposable capillary cell. Particles size was determined by dynamic light scattering (DLS) at a detection angle of 173º by using the Cumulants analysis and the Stokes-Einstein equation for colloidal dispersions:

$$D = \frac{K_B T}{6\pi\eta r} \qquad (1)$$

Where D the translational diffusion coefficient, K_B the Boltzmann's constant, T the thermodynamic temperature, η the dynamic viscosity and r is the hydrodynamic diameter.

The zeta potential of the AuMSS was calculated by using the Smoluchowski model (equation 2) included in the Zetasizer software (v 7.03).

$$U_E = \frac{2\varepsilon\zeta\, f(Ka)}{3\eta} \quad (2)$$

Where ζ is the zeta potential, U_E the electrophoretic mobility, ε the dielectric constant, f(Ka) Henry's equation and η the dynamic viscosity.

2.2.5.3. Ultraviolet-visible spectroscopy analysis

The success of the AuMSS nanopheres synthesis was evaluated by acquiring the UV-vis spectra in a UV-Vis spectrophotometer (Thermo Scientific Evolution™ 201 Bio UV-vis Spectrophotometer, Thermo Fisher Scientific Inc., USA). The UV-vis spectra of the coated and uncoated AuMSS nanoparticles were recorded at 300 nm/min scanning rate, with a wavelength range from 200 to 1100 nm.

2.2.5.4. Fourier transform infrared spectroscopy analysis

FTIR spectroscopy was used to evaluate the success of the AuMSS nanospheres purification process (*i.e.* the CTAB removal), as well as the successful attachment of the polymers on the particle surface. For that purpose, FTIR spectra of the nanoparticles were acquired on a Nicolet iS10 spectrometer, with a 4 cm^{-1} spectral resolution from 4000 to 600 cm^{-1} (Thermo Scientific Inc., Massachusetts, USA). A baseline correction was performed to avoid possible interferences in the FTIR spectra. Data analysis was executed in the OMNIC spectra software (Thermo Scientific).

2.2.5.5. Thermogravimetric analysis

The polymer content on the different AuMSS nanospheres formulations was measured by performing the thermogravimetric analysis (TGA) of the samples. Briefly, uncoated or coated AuMSS nanospheres were heated up to 600 °C, at a heating rate of 10 °C/min, under an inert atmosphere on SDT Q600 equipment (TA Instruments, USA) and the weight losses were recorded along time.

2.2.6. Biocompatibility assays

2.2.6.1. Cell viability

The biocompatibility of uncoated and coated AuMSS nanospheres was evaluated by incubating them with HeLa cells and measuring the cell viability through a resazurin-based assay at different time periods. This method uses a non-toxic reagent (resazurin), which when inside the cells becomes reduced from a non-fluorescent blue resazurin compound to the fluorescent pink-reddish resorufin (200). This transformation occurs through the action of mitochondrial enzymes such as flavin mononucleotide dehydrogenase and nicotinamide adenine dehydrogenase (200).

The HeLa cells were seeded in 96-well flat bottom culture plates at a density of 10000 cells per well, with 100 µL of culture medium (DMEM-HG) during 48 h, at 37 °C, in a humidified atmosphere containing

5% CO_2. After that time, cells were incubated with different concentrations of uncoated or coated AuMSS nanoparticles, from 25 to 200 µg/mL. After 24, 48 and 72 h of incubation, the medium was replaced with 110 µL of 10% (v/v) resazurin solution and incubated for 4 h. The produced resorufin fluorescence was quantified with a spectrofluorometer (Spectramax Gemini XS, Molecular Devices LLC, USA) at an excitation/emission wavelength of λex=560 nm and λem=590 nm. Cells incubated with absolute EtOH were used as a positive control (K^+), whereas cells without being exposed to nanoparticles were used as a negative control (K^-).

2.2.6.2. Evaluation of the AuMSS effects on the cell migration ability

The biocompatibility of uncoated or coated AuMSS nanospheres was also evaluated by assessing their effect on the HeLa cells migration ability. For that purpose, 50000 HeLa cells were seeded in a 24 multi-well flat bottom plate with 2 mL of DMEM-HG. The plate was incubated at 37 °C in a humidified atmosphere with 5% CO_2 until reach cell confluence. After this time, the medium was removed, a scratch was created in the middle of each well using a micropipette tip, and the wells were washed with PBS to remove non-adherent cells. Then, different concentrations of uncoated or coated AuMSS nanospheres were incubated (50, 100 and 150 µg/mL), whereas cells non-exposed to nanoparticles were used as a control. At predetermined time points (0, 24, 48, and 72 h), optical images were captured by using an Olympus CX41 inverted optical microscope equipped with an Olympus SP-500 UZ digital camera and the cell migration distance was measured using image J software (Image J 2.0.0, NIH Image, USA).

2.2.6.3. Hemolysis

Hemolysis experiments were performed according to a protocol previously published in the literature (201). EDTA stabilized blood samples were freshly obtained from adult mice. Initially, the whole blood samples were centrifuged at 500g, for 5 min, at 4 °C to recover the red blood cells (RBCs). Then, the RBCs were washed three times with NaCl solution (150 mM) and then were diluted in PBS, distributed by the test tubes and centrifuged. Subsequently, 1 mL of AuMSS or AuMSS+Polymer 25/75, 50/50 and 75/25 solutions in PBS at different concentrations (100, 150 and 200 µg/mL) were added to the RBC suspension. Moreover, positive (K^+) and negative (K^-) control samples were prepared by adding 1 mL of Triton-X 100 and PBS, respectively. Then, the samples were incubated at room temperature for 2 h. The samples were slightly shaken once for every 30 min to resuspend the RBCs and particles. After the incubation period, the samples were centrifuged at 500g for 5 min, at 4 ºC and 100 µL of the supernatant were transferred to a 96-well plate to measure the hemoglobin absorbance at 570 nm. RBCs hemolysis percentage was calculated using the equation:

$$\text{Hemolysis (\%)} = \frac{\text{Sample Abs} - \text{Negative Control Abs}}{\text{Positive Control Abs} - \text{Negative Control Abs}} \qquad (3)$$

2.2.7. Cellular uptake by HeLa cells

The uptake of AuMSS and AuMSS+Polymer nanoparticles by HeLa cells was assessed by fluorescence spectroscopy, by adapting a method previously described in the literature (202). Briefly, HeLa cells were seeded at a density of 10000 cells per well in 96-well flat bottom culture plates, and then cultured at 37 ºC in a humid atmosphere containing 5% CO_2 for 24 h. Subsequently, cells were exposed to 200 µg/mL of FITC-tagged AuMSS or AuMSS+Polymer for 4 h, washed with ice-cold Krebs Ringer Buffer (KRB) and lysed with 1% Triton X-100 (for 30 min, at 37 °C). Then, the FITC fluorescence was quantified with a spectrofluorometer (Spectramax Gemini XS, Molecular Devices LLC, USA) at an excitation/emission wavelength of λex=480 nm and λem=570 nm. Cells only incubated with KRB were used as a negative control.

To further confirm the uptake results, Confocal Laser Scanning Microscopy (CLSM) was performed to evaluate the nanoparticles internalization by HeLa cells. For that purpose, 20000 HeLa cells were seeded on µ-Slide 8 well Ibidi imaging plates (Ibidi GmbH, Germany), then incubated at 37 ºC in 5% CO_2 humidified atmosphere. After 24 h, cells were exposed to FITC stained AuMSS and AuMSS+Polymer nanospheres, using a concentration of 200 µg/mL, for 4 h. After incubation, cells were washed with PBS, fixed with paraformaldehyde 4% (w/v), for 15 min at room temperature, and rinsed again with PBS 1%. Subsequently, cells were treated with WGA-Alexa Fluor® 594 (for 30 min at room temperature and washed several times with PBS 1%) for cell cytoplasm staining, and the cell nucleus was labeled with Hoechst 33342® (for 20 min at room temperature and washed several times with PBS 1%). Imaging experiments were performed in multi-track mode on a confocal microscope (Zeiss LSM 710, Carl Zeiss, Germany) equipped with a Plan Apochromat 63x/1.4 Oil Differential Interference Contrast objective, where consecutive z-stacks were acquired. 3D reconstructions and image analysis were performed in Zeiss Zen 2010 software.

2.2.8. Statistical analysis

Statistical analysis of the obtained results was performed using GraphPad Prism v.5.0 software (Trial version, GraphPadSoftware, CA, USA). Data are presented as the mean ± standard deviation (s.d.). One-way analysis of variance (ANOVA) with the Student–Newman–Keuls test was used to compare different groups. A value of p lower than 0.05 was considered statistically significant.

Chapter 3

Results and Discussion

3. Results and Discussion

3.1. Synthesis and characterization of PEOZ and β-CD modified with TESPIC

The PEOZ and β-CD polymers were selected to prevent the Au-MSSs uncontrolled drug release profile, enhance nanoparticle blood circulation time and ultimately potentiate the therapeutic effect of this nanosystem. PEOZ display a high solubility in water, it is biocompatible, biodegradable and presents a good temperature stability (203, 204). Further, PEOZ also provides a steric barrier to the nanocarrier in a similar way to PEG (205). The reduction of the unspecific adsorption of serum proteins to nanoparticles surface is essential to reduce their uptake by the RES and consequently increase their blood circulation time (206). Therefore, the probability of the nanoparticles to reach the tumor region, extravasate through their defective vasculature and exert the therapeutic effect is enhanced (207-211). On the other side, β-CDs are cyclic oligosaccharides (7 glucose units) with lipophilic inner cavities and hydrophilic outer surfaces. Up to now, the cyclodextrins have been used as gatekeepers or pore blockers on mesoporous silica nanoparticles, due to their size (around 1.5 nm) which matches the silica pore diameters (212). Therefore, the inclusion of these pore blockers at the surface of the nanoparticle can decrease the drug leakage during the blood circulation, decrease their interaction with healthy cells and consequently reduce the side effects associated with therapies (213, 214). To allow the PEOZ and β-CD attachment to the AuMSS surface, these polymers were chemically modified, by linking the TESPIC to the polymer backbone through a hydrogen-transfer nucleophilic addition reaction (Figure 3.1).

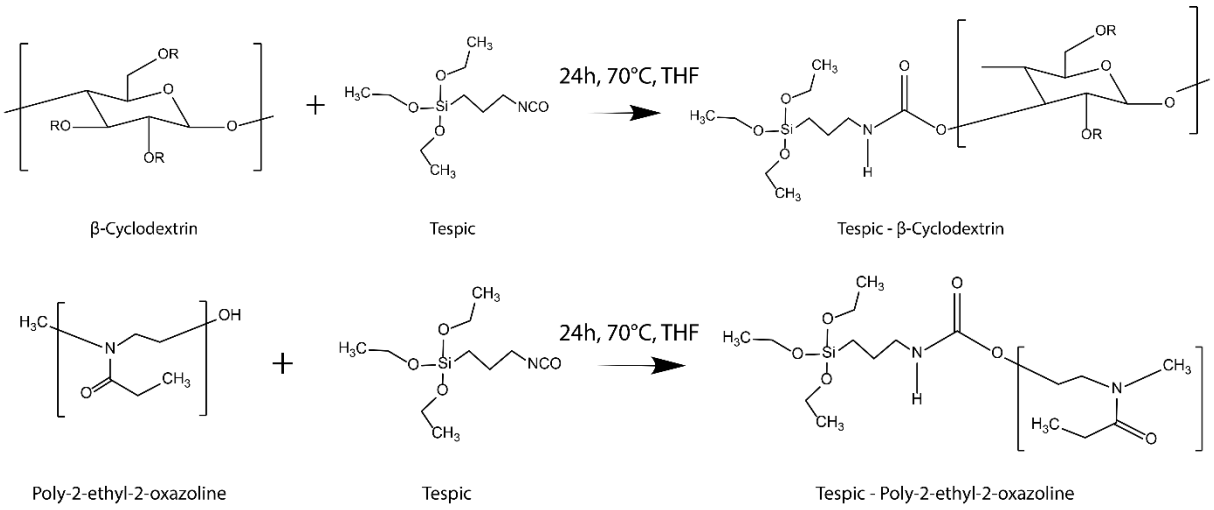

Figure 3.1. Representation of the PEOZ and β-CD silane derivatives synthesis procedures.

The successful modification of PEOZ and β-CD was confirmed by FTIR (Figure 3.2 B). The PEOZ spectra show a characteristic peak at 1650 cm^{-1} corresponding to the amide bond, and at 2900 cm^{-1} attributed to the C-H stretch (215). After the modification with TESPIC, the PEOZ spectra showed an additional peak at 1100 cm^{-1} attributed to the Si-O-C groups of TESPIC (26). In the β-CD spectra, it is possible to observe the OH, CH_2 and C-C characteristic peaks at the 3300 cm^{-1}, 2900 cm^{-1} and 1000 cm^{-1} region (216). The β-CD modification with TESPIC resulted in the modification of the FTIR spectra being observed a peak at 1620 cm^{-1} that correspond to the formation of a secondary amide and

a modification in the 1100 cm^{-1} peak corresponding to the Si-O-C group TESPIC. These alterations in the FTIR spectra indicate the successful modification of PEOZ and β-CD polymers with TESPIC which allows their application in the AuMSS nanospheres functionalization.

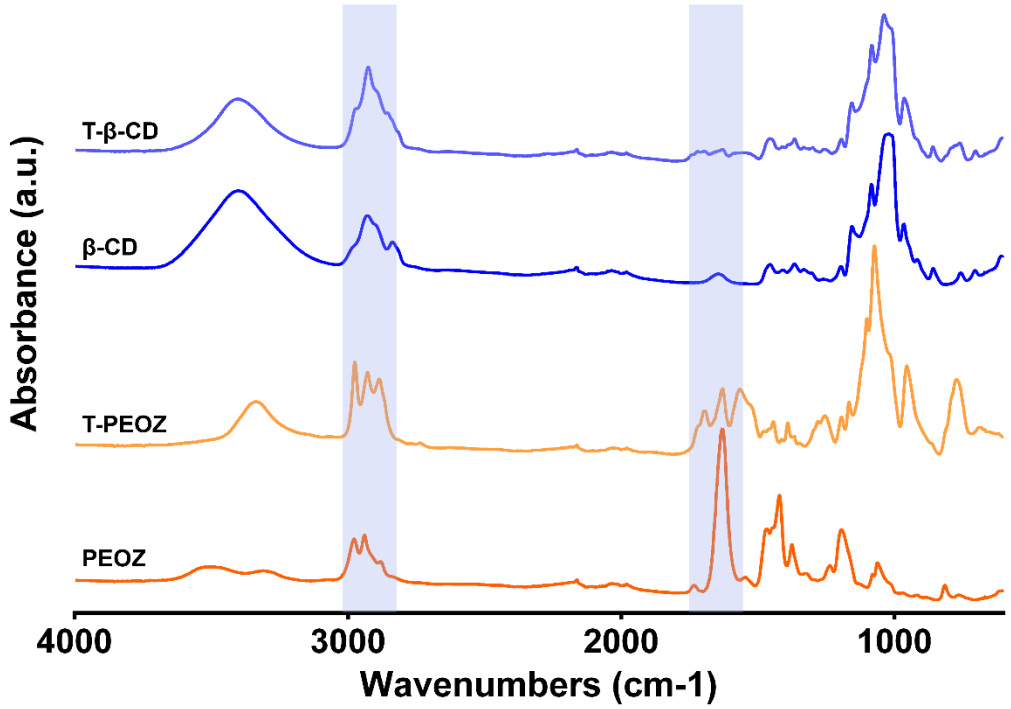

Figure 3.2. FTIR spectra of PEOZ, TESPIC-PEOZ (T-PEOZ), β-CD, and TESPIC- β-CD (T- β-CD) polymers.

3.2. Synthesis and characterization of the nanoparticles

The AuMSS were synthesized by adapting a method previously described in the literature (75). The synthesis procedure of AuMSS is a straightforward process that can be divided into two main phases: the production of the spherical gold nucleus and the coating with a mesoporous silica shell (Figure 3.3 A). In the first step, an alkaline solution containing CTAB and the gold precursor ($HAuCl_4$) is reduced by formaldehyde, to originate CTAB-stabilized gold nanosized spheres. Subsequently, the silica shell is produced by adding TEOS, which is hydrolyzed (*i.e.* removal of the TEOS alkoxy group)

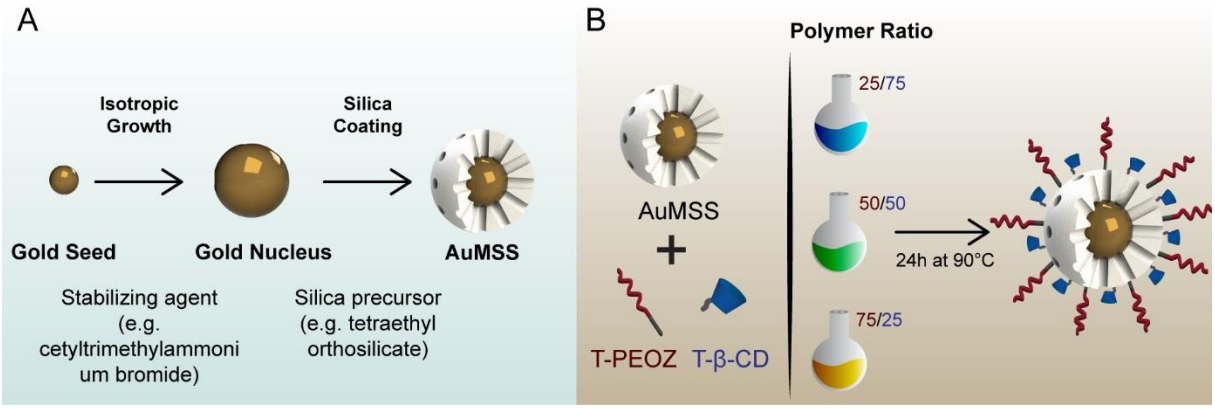

Figure 3.3. Representation of the AuMSS and AuMSS+Polymer nanospheres synthesis. A) Production of AuMSS nanospheres. B) Functionalization of AuMSS with different T-PEOZ and T-β-CD ratios (25/75, 50/50 and 75/25).

and forms through a condensation reaction (*i.e.* creation of siloxane bonds Si-O-Si) a mesoporous shell around the gold nucleus. At this point, the CTAB works as a pore template surfactant for TEOS condensation around the gold cores and, thus, leads to the formation of a core-shell based nanostructure. Then, a purification step must be performed to remove the cytotoxic CTAB molecules. For this purpose, two different methodologies are normally applied, the nanoparticles calcination or a solvent extraction protocol (123). However, the utilization of calcination methods, CTAB pyrolysis at 400-500 °C, often lead to the loss of the surface silanol groups that are essential to the subsequent modifications of the nanoparticle (217). Therefore, a solvent-based extraction protocol was used herein. In this approach, an acid/alcohol mixture was used to promote the CTAB removal by electrostatic repulsion since in acidic pH, the cationic CTAB molecules are repelled by the silica positive charge (217)]. The nanoparticles organization in core-shell structure is a simple approach that allows the combination of different functions, such as drug delivery, targeting, and imaging in a single system. In this nanosystem, the gold nucleus allows their application as an imaging agent, specifically as contrast agents for MRI and CT, whereas the mesoporous silica shell stabilizes and protects the gold core, adds a drug reservoir to encapsulate biomolecules and allows posterior modifications for improving the nanoparticles blood circulation time and accumulation in the tumor tissue.

The produced AuMSS nanospheres were characterized by TEM, to assess the particles morphology as well as the successful organization in a gold core with a uniform silica shell. Furthermore, DLS was used to assess the nanoparticles size (Figure 3.4 and 3.5). The obtained AuMSS nanoparticles were homogeneous and presented a spherical morphology (Figure 3.4 A1). The TEM images showed the particle organization in a gold core (darker central region of the nanoparticles, which results from the higher density of the gold) and a mesoporous silica shell (the lighter outer region of the nanoparticles). On the other side, the AuMSS nanospheres size characterization by DLS showed that the nanospheres had an average diameter of 100±5 nm (Figure 3.4 A2 and 3.5 A). Subsequently, the AuMSS were functionalized with different ratios of PEOZ and β-CD (25/75, 50/50 and 75/25) by promoting its condensation at the particle surface (Figure 3.3 B and Figure 3.4 B1, C1, and D1). The DLS size measurements revealed that the nanoparticles surface functionalization increased their overall size to 123±8, 152±9 and 160±27 nm for AuMSS+Polymer 25/75, 50/50 and 75/25, respectively (Figure 3.4 B2, C2, D2, and 3.5 A). Such variation in the nanoparticles' size indicates the successful binding of the PEOZ/β-CD polymers to the surface of the nanoparticles. Nevertheless, the nanoparticles overall size still allows their administration in the blood stream as well as their passive accumulation in the tumor tissue by exploiting the leaky structure of the tumoral vasculature, *i.e.* the EPR effect (32, 218).

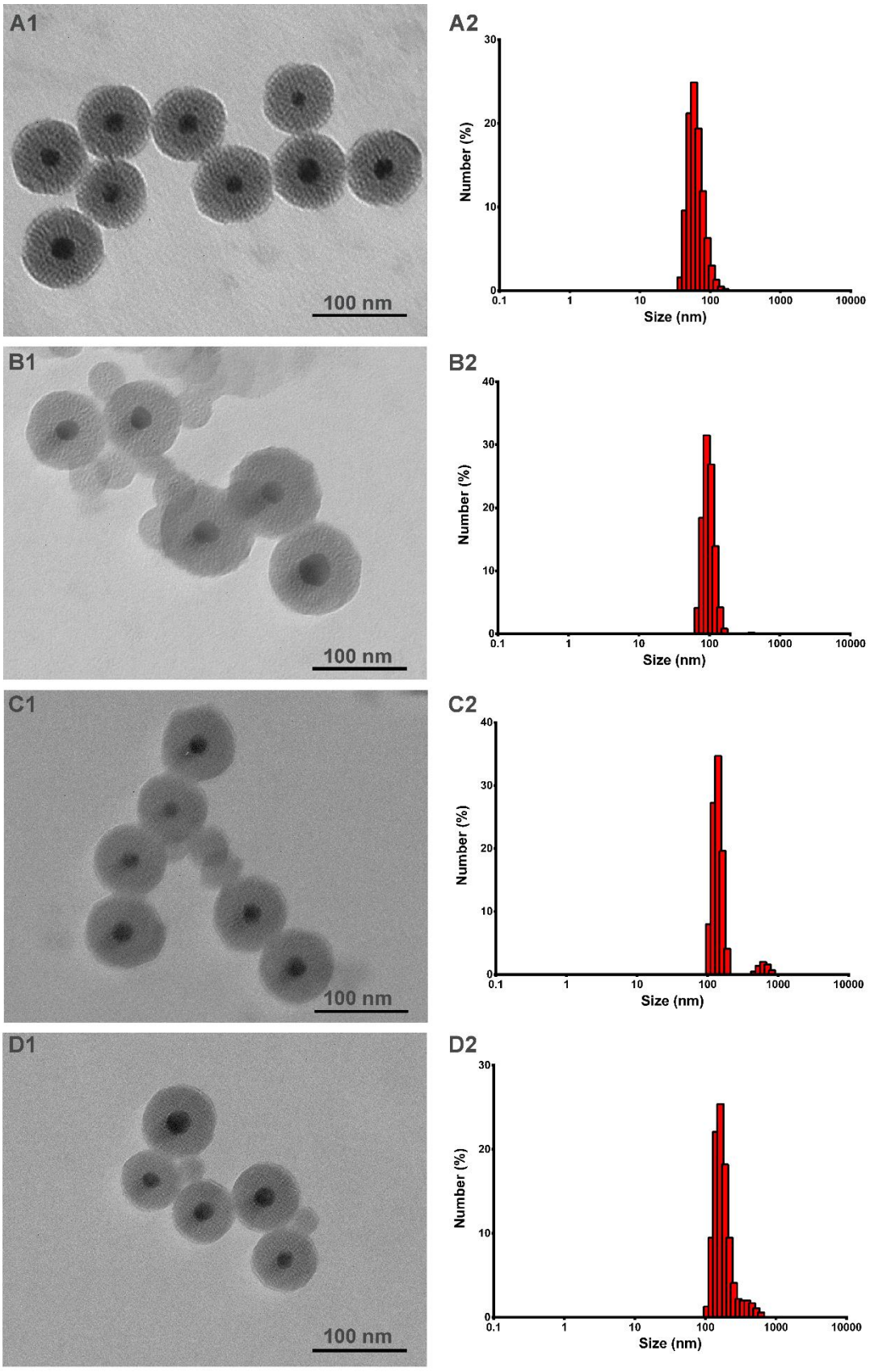

Figure 3.4. AuMSS and AuMSS+Polymer nanospheres morphology (A1-D1) and size analysis (A2-D2). TEM images and DLS size distribution by number of AuMSS (A), AuMSS+Polymer 25/75 (B), AuMSS+Polymer 50/50 (C), and AuMSS+Polymer 75/25 (D) nanospheres.

On the other hand, the surface charge measurements were also carried out to further characterize the nanoparticles surface functionalization. The obtained results show that the non-coated AuMSS nanospheres display a zeta potential of -26.6±1.2 mV, whereas the coated nanoparticles presented a less negative surface charge, -17.4±0.8, -14.2±0.2, and -7.2±0.8 mV for 25/75, 50/50, and 75/25 PEOZ/β-CD ratio, respectively (Figure 3.5 B). The negatively surface charge of non-coated AuMSS nanospheres is attributed to the silanol groups present at the particle surface. Further, the neutralization of the nanoparticles surface charge can be justified by the loss of the silanol groups on the AuMSS surface (*i.e.* polymers are grafted by a condensation reaction with the surface silanol groups) (219, 220). The nanoparticles surface charge has a high impact on their blood circulation time and biocompatibility (221, 222). In fact, neutral surface charges (±10 mV) are often considered ideal for biological applications and nanoparticles with slightly negative surface charge often present increased blood circulation times, since their interactions with blood cellular components and serum proteins are decreased (56).

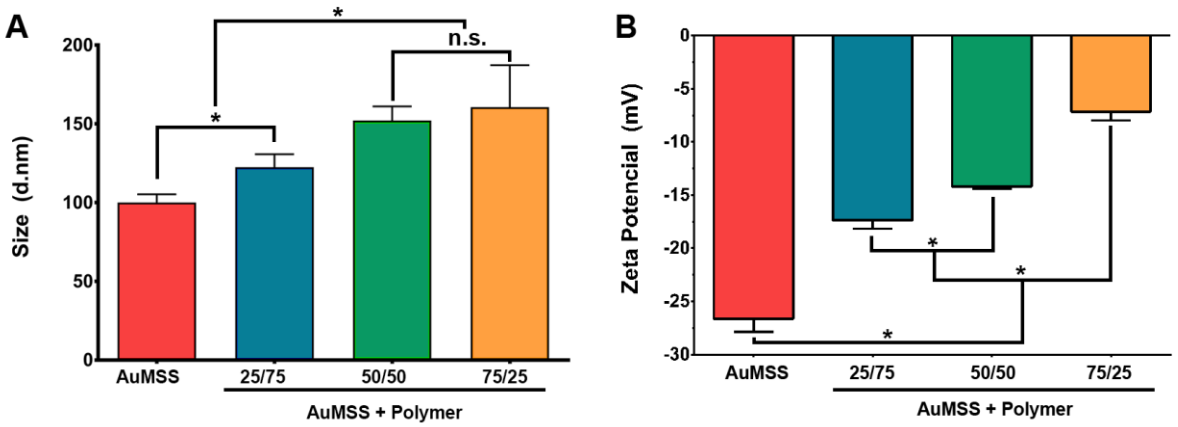

Figure 3.5. Size (A) and zeta potential (B) analysis of AuMSS and AuMSS+Polymer 25/75, 50/50, and 75/25 nanospheres. Data are presented as mean ± s.d., * $\rho<0.05$, n = 5.

The AuMSS and AuMSS+Polymer 25/75, 50/50, and 75/25 nanospheres FTIR characterization was carried out for assessing the formation of the mesoporous silica coating and the successful functionalization with PEOZ and β-CD polymers (Figure 3.6). The FTIR spectra of AuMSS nanospheres shows three characteristic peaks in the 1100 to 750 cm^{-1} region that corresponds to Si-O-Si, Si-O, and Si-OH vibrations confirming the presence of the mesoporous silica shell (26). Furthermore, after the nanoparticles functionalization (*i.e.* grafting of the PEOZ and β-CD) it was possible to observe the presence of additional peaks corresponding to the polymers. The AuMSS+Polymer 25/75, 50/50, and 75/25 nanospheres showed the PEOZ and β-CD characteristic peaks at the 1600 cm^{-1} and 2900 cm^{-1} region, corresponding to the amide bond and C-H stretch (223, 224). Additionally, all the functionalized AuMSS nanospheres showed an increase in the ratio between the Si-O-Si peak at 1045 cm^{-1} and Si-OH peak at 950 cm^{-1}, which occurs due to the PEOZ and β-CD silane derivatives condensation with the silanol groups on the mesoporous silica surface. These results indicate the successful attachment of the polymeric chains to the particle surface.

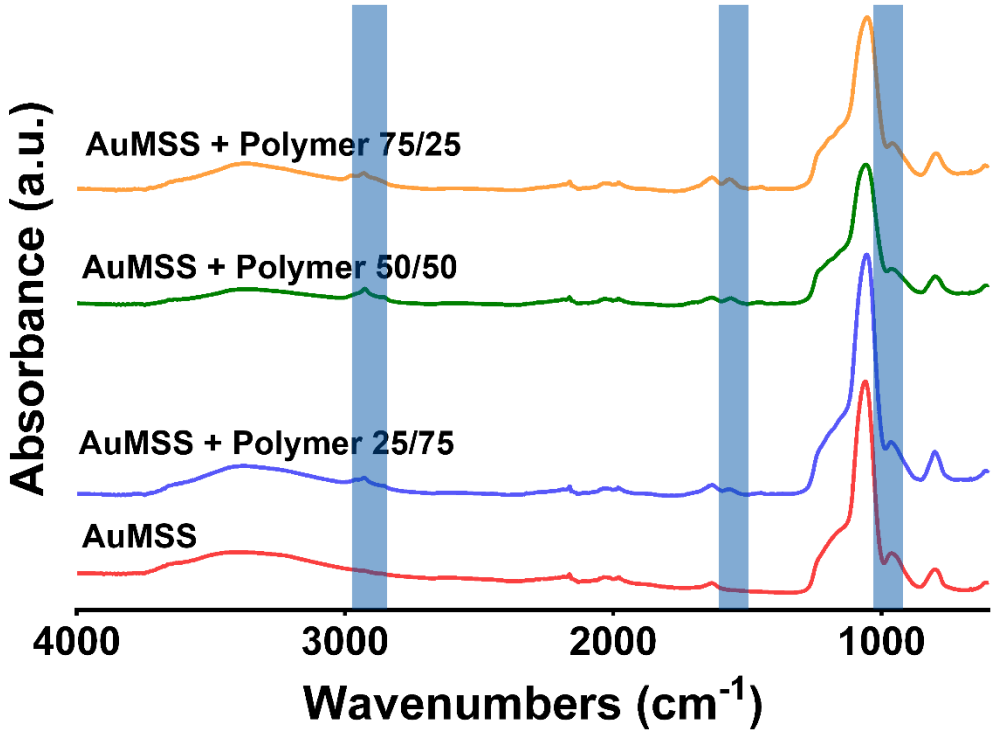

Figure 3.6. FTIR spectra of AuMSS and AuMSS+Polymer 25/75, 50/50, and 75/25 nanospheres.

Therefore, to determine the polymeric content in the AuMSS nanospheres a TGA analysis was performed (Figure 3.7 A). In this study due to the inorganic nature of AuMSS nanospheres, it is expected that only the PEOZ and β-CD polymers will suffer pyrolysis. The recorded weight losses for non-coated AuMSS nanospheres were minimal and can be attributed to the loss of the hydroxyl groups on the external surface of the particles or to the evaporation of water adsorbed in the interior region of the mesopores. On the other side, the functionalized AuMSS nanospheres presented a weight loss of 13.5%, 15.2%, and 17% for the 25/75, 50/50 and 75/25 ratios, respectively. These results clearly show the successful attachment of the polymers to the surface of AuMSS nanospheres. Further, it also was observed a higher polymer content on AuMSS nanoparticles with the increase of the PEOZ ratio, which can be attributed to the higher packing density of the PEOZ allowing a higher number of polymer chains to be linked on the particle surface.

Finally, to confirm that the gold core does not suffer any degree of degradation during the CTAB removal and surface functionalization procedures, UV-vis spectra of AuMSS, AuMSS+Polymer 25/75, 50/50, and 75/25 nanospheres were acquired (Figure 3.7 B). The UV-vis spectra of all the AuMSS formulations show the characteristic peaks of the spherical gold core in the 550 nm region (Figure 3.7 B) (75). Such results confirm that the gold core remains intact throughout the particles synthesis indicating that the potential of these nanoparticles to be applied as imaging agent remain intact (*i.e.* contrast agent for MRI and CT).

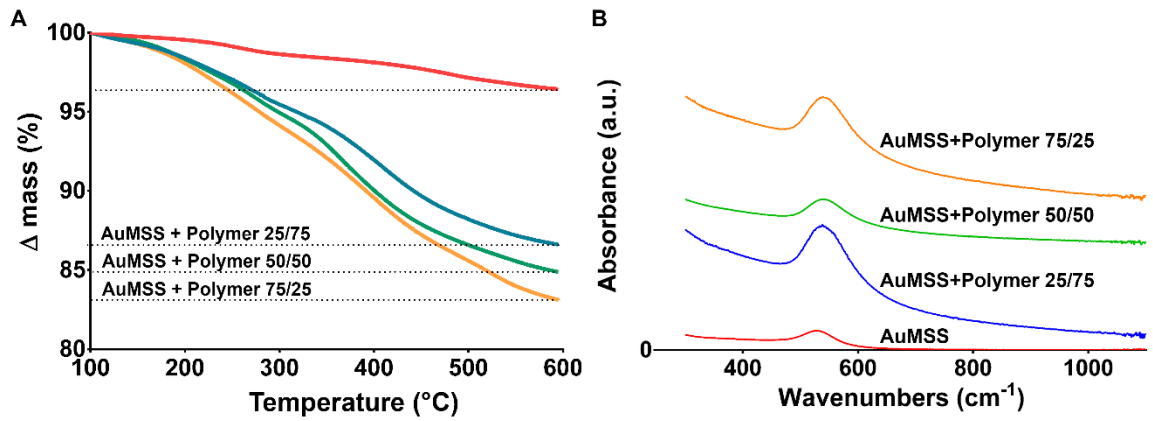

Figure 3.7. Physicochemical characterization of AuMSS nanospheres. TGA (A) and UV-vis spectra analysis (B) of AuMSS, AuMSS+Polymer 25/75, 50/50, and 75/25 nanospheres.

3.3. Characterization of the AuMSS cytocompatibility

The nanoparticles cytocompatibility is fundamental to allow their application in the biomedical field. Herein, the AuMSS, AuMSS+Polymer 25/75, 50/50, and 75/25 nanospheres effect on the cell motility and hemolysis rate were assessed in order to determine the maximum dose that can be administered in the body and also confirm the possible protective effect of the polymeric surface functionalization.

3.3.1. AuMSS biocompatibility

The biocompatibility of AuMSS nanospheres and its coated derivatives was evaluated using cervical cancer HeLa cells as model. For that purpose, the different nanoparticle formulations were incubated for 24 and 48 h, at concentrations ranging from 25 up to 200 µg/mL, and then the cellular viability was studied using the resazurin assay (Figure 3.8).

The obtained results show that the non-coated AuMSS nanospheres are biocompatible at concentrations up to 175 µg/mL. A decrease in the cell viability to values inferior to 70% was observed when cells were incubated with 200 µg/mL of nanoparticles (Figure 3.8 A). On the other side, the AuMSS functionalization with PEOZ and β-CD improved the nanoparticles biocompatibility, all the formulations presented a cellular viability superior to 70% even when concentrations of 200 µg/mL of nanoparticles were used (Figure 3.8 B, C, and D). However, it is important to notice that after 48 h of incubation, the AuMSS+Polymer 50/50 formulation (at 200 µg/mL) presented a cell viability value around the 75-80%. The ISO 10993-5 states that a material has a cytotoxic effect when the cell viability is reduced by more than 30%. Therefore, these results indicate that the inclusion of the polymers increases the nanoparticles biocompatibility. Furthermore, these findings are in accordance with several reports available in the literature based on AuMSS derived nanosystems (162, 225).

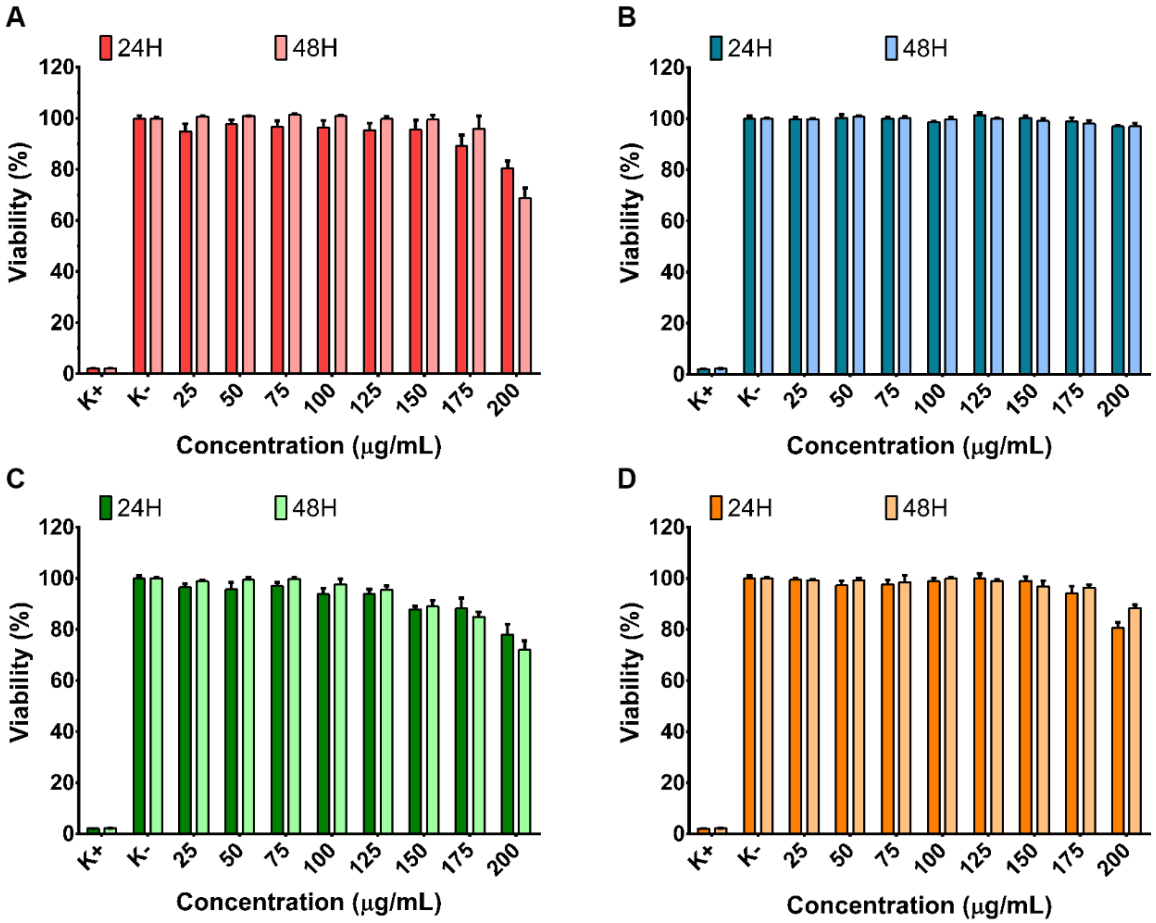

Figure 3.8. Characterization of the cellular viability after incubation with different concentrations of nanoparticles for 24 and 48 h. Biocompatibility analysis for AuMSS A), AuMSS+Polymer 25/75 B), AuMSS+Polymer 50/50 C) and AuMSS+Polymer 75/25 D). Positive control (K+): cells treated with EtOH; negative control (K-): cells without nanoparticles incubation. Data are presented as mean ± s.d., * $\rho<0.05$, n = 5.

3.3.2. Characterization of the AuMSS effect on cell migration

In order to complement the data obtained in the resazurin assay, the AuMSS cytocompatibility was further characterized by evaluating the nanoparticles effect on the HeLa cells motility (Figure 3.9). The obtained results reveal that the cell gap was almost closed after 72 h of cells being incubated with all formulations, even when the highest concentration of nanoparticles was tested (200 μg/mL). Such results indicate that the cells exposed to the AuMSS nanospheres were able to adhere and proliferate in a similar way to the negative control. Further, no significant alterations in cell morphology were observed in the microscopy images (Figure 3.9 B). These findings clearly demonstrate the biocompatibility of the produced nanomaterials.

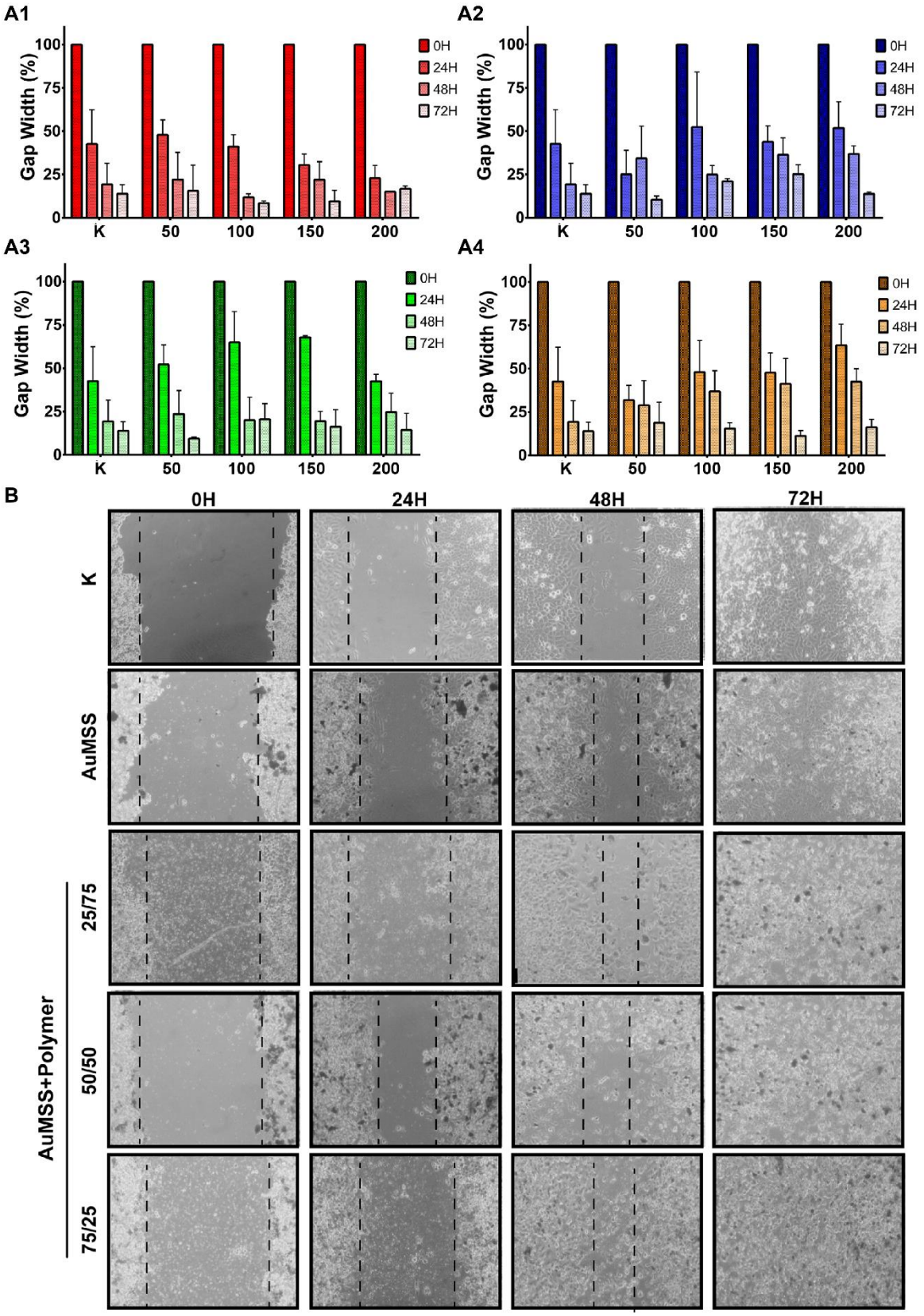

Figure 3.9. Characterization of cell migration behavior when they are seeded in contact with the produced nanoparticles. Analysis of AuMSS (A1); AuMSS+Polymer 25/75 (A2); AuMSS+Polymer 50/50 (A3) and AuMSS+Polymer 75/25 (A4) nanospheres effect on HeLa cells migration behavior at 0, 24, 48 and 72 h of incubation. (K) Cells non-exposed to nanoparticles. B) Cell migration assay: optical images at 10x magnification of Control, AuMSS; AuMSS+Polymer 25/75; AuMSS+Polymer 50/50 and AuMSS+Polymer 75/25 test groups (200 µg/mL) at 0, 24, 48 and 72 h.

3.3.3. Characterization of the hemolysis effect triggered by AuMSS nanoparticles

The AuMSS nanospheres are intended to be intravenouly administrated in the human body, therefore the evaluation of their biocompatibility with the blood components is an essential step during the preclinical development. Hemolysis in the humans can lead to anemia, jaundice and other pathologies (226). With that in mind, the possible protective role of the PEOZ and β-CD inclusion on the AuMSS nanospheres was evaluated by studying the nanoparticles hemocompatibility (Figure 3.9 A). For that purpose, the erythrocytes lysis was quantified upon incubation with AuMSS nanospheres at different concentrations (100, 150, and 200 µg/mL). The obtained results show that both the non-coated and coated AuMSS nanospheres are non-hemolytic, presenting hemolysis rates inferior to 5% (Figure 3.9 B). Although, it is worth to notice that the AuMSS+Polymer 50/50 and 75/25 formulations presented a smaller hemolysis degree, with less than 1% of hemoglobulin released even when the higher concentrations of nanoparticles (200 µg/mL) were used. Such results indicate an additional protective effect with the inclusion of PEOZ and β-CD on the nanoparticles surface, which can be attributed to the nanoparticles surface charge neutralization with the increased content of PEOZ. The obtained data is in accordance with the guidelines established by international agencies (ISO/TR 7406) regarding the critically safe hemolytic ratio as well as with similar studies available in the literature where the polymeric functionalization of the nanoparticles improved its hemocompatibility (198, 201, 227).

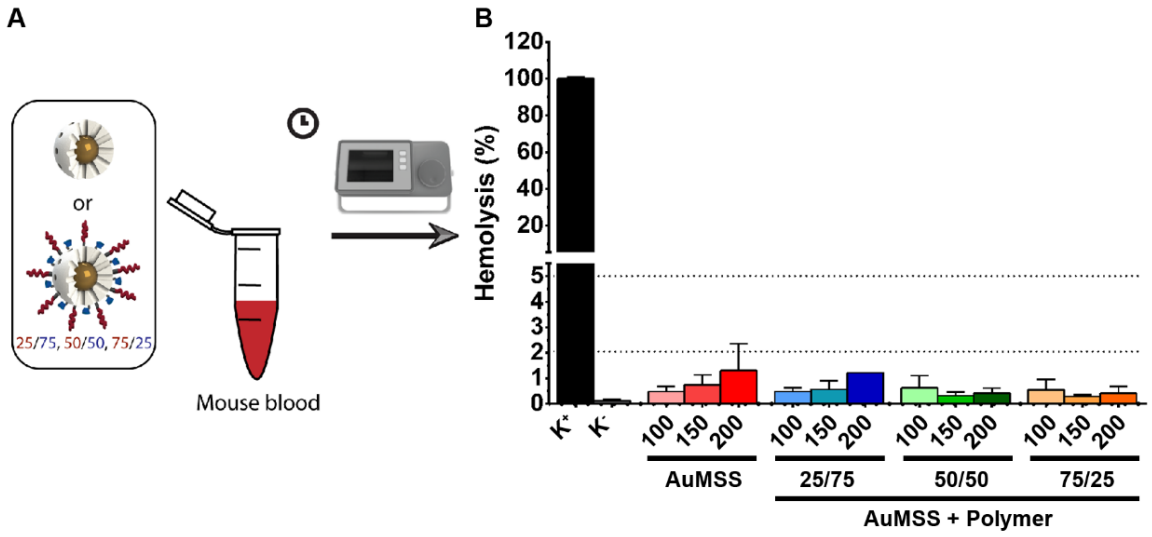

Figure 3.10. Hemocompatibility analysis of the AuMSS nanospheres. A) Schematics of the hemocompatibility analysis methodology. B) Analysis of the RBCs lysis upon incubation with different concentrations of non-coated or coated AuMSS nanospheres. Data are presented as mean ± s.d., *p<0.05, n =3.

3.3.4. AuMSS uptake in HeLa cells

After assessing the biocompatibility of the AuMSS derivatives, the uptake of AuMSS and AuMSS+Polymer nanoparticles by HeLa cancer cells was evaluated by CLSM and fluorescence

spectroscopy (Figure 3.11 A). The tracking of non-coated or coated AuMSS nanospheres was achieved by staining the particles with FITC. Then, AuMSS and AuMSS+Polymer 25/75, 50/50, and 75/25 were incubated 4 h with HeLa cells and confocal images were acquired. The CLSM images (Figure 3.12) show the nanoparticles in the cytoplasm of HeLa cancer cells. Moreover, the images also show that the AuMSS+Polymer 25/75, 50/50, and 75/25 formulations were the ones that were more internalized by HeLa cancer cells.

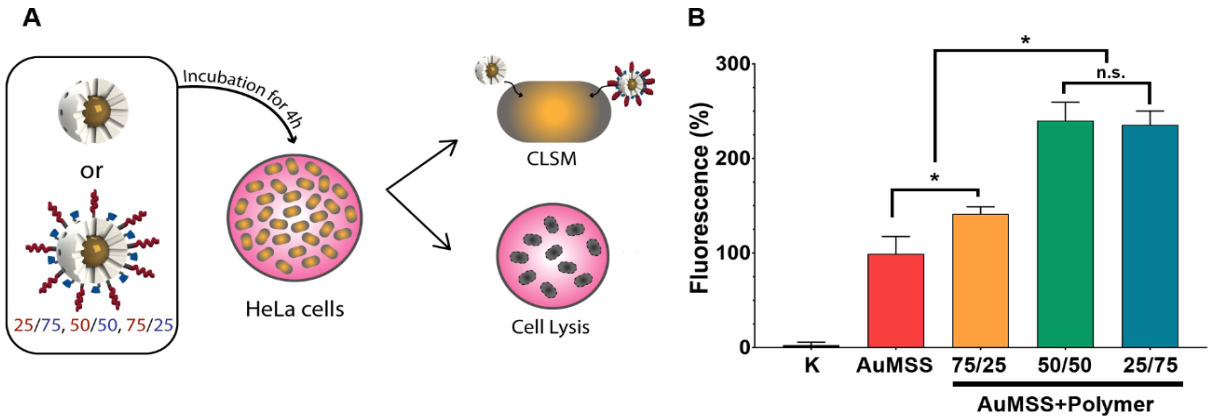

Figure 3.11. Analysis of AuMSS nanospheres uptake by HeLa cells after 4 h of incubation. (A) Schematics of uptake experiments. (B) Fluorescence spectroscopy analysis of AuMSS and AuMSS+Polymer uptake by HeLa cells, fluorescence was normalized towards AuMSS group. Data are presented as mean ± s.d., *p<0.05, n = 5.

Furthermore, the fluorescence of AuMSS or AuMSS+Polymer 25/75, 50/50, and 75/25 nanospheres on HeLa cells after 4 h of incubation was measured through fluorescence spectroscopy. The fluorescence spectroscopy studies revealed that when compared to the AuMSS nanospheres, the inclusion of the PEOZ/β-CD polymeric coating improved the nanoparticles uptake, 236±15, 240±20, and 142±8% for the AuMSS+Polymer 25/75, 50/50 and 75/25 nanospheres, respectively (Figure 3.11 B). These results are in accordance with the CLSM data. In fact, despite the small variation in the surface charge of AuMSS+Polymer 25/75, 50/50 and 75/25 nanospheres, the differences observed in the nanoparticles uptake can be attributed to the smaller size of 25/75 and 50/50 formulations, leading to an increased uptake rate by HeLa cancer cells (228). Nevertheless, the obtained results show that AuMSS+Polymer are efficiently internalized by HeLa cells and can deliver their content in the cytoplasm of the cell to exert the desired therapeutic effect, thus avoiding the drug premature degradation in the extracellular medium. Furthermore, the superior uptake rate of AuMSS+Polymer nanospheres also highlights a superior capacity to bypass different cellular drug efflux pathways or even intracellular drug degradation events that limit the drug therapeutic effect in the interior of the cancer cells.

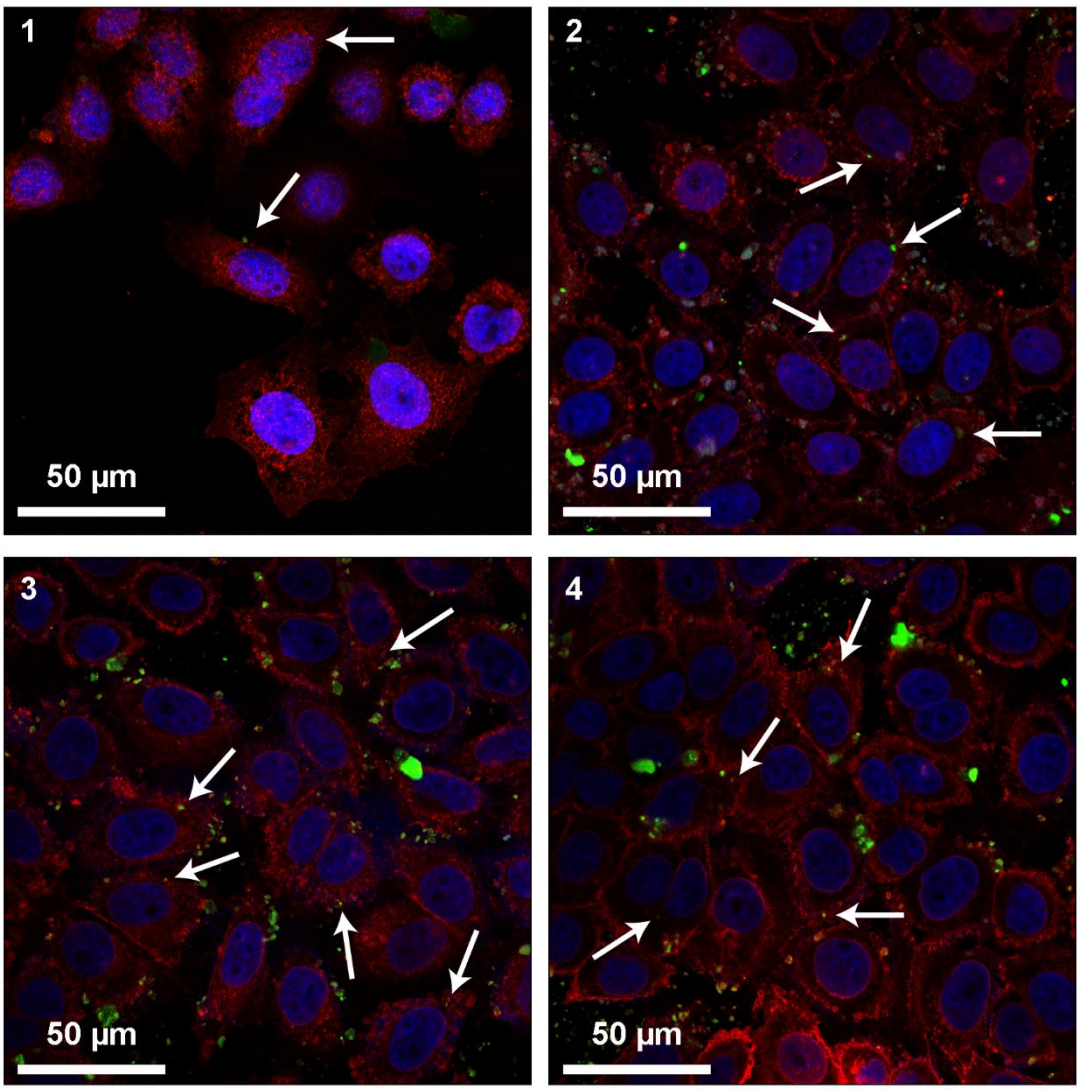

Figure 3.12. AuMSS nanospheres internalization by HeLa cancer cells. CLSM images of FITC stained AuMSS A); AuMSS+Polymer 25/75 B); AuMSS+Polymer 50/50 C) and AuMSS+Polymer 75/25 D) nanospheres uptake after 4 h of incubation with HeLa cells. Blue channel: cell nucleus; Red channel: cell cytoplasm; Green channel: FITC stained non-coated or coated AuMSS nanospheres.

Chapter 4

Conclusion and Future Perspectives

4. Conclusion and future perspectives

Nowadays there is a huge demand for novel and more effective anti-cancer therapeutics. The recent breakthroughs in the nanotechnology field triggered a new era of anti-cancer medicines. Among the plethora of nanoparticles that have been developed so far, the AuMSS nanoparticles display advantageous physicochemical and biological properties that make them promising nanoplatforms for cancer therapy.

The AuMSS nanospheres have the potential to simultaneously act as chemotherapeutic and imaging agents. The nanomedicines application in cancer therapy are highly dependent on their blood circulation time and drug release profile. Herein, PEOZ and β-CD were combined for the first time to functionalize AuMSS nanospheres with the objective to increase the nanoparticles biological performance. PEOZ provides a steric barrier to the nanoparticles, which decreases the protein corona and consequently enhance the nanoparticles blood circulation time. The β-CDs due to their size (around 1.5 nm) match the silica pore diameters and were used here to act as gatekeepers or pore blockers for decreasing the drug leakage from AuMSS during the blood circulation as well as decrease the drug side effects.

The obtained results demonstrate the successful production of PEOZ and β-CD silane derivatives by reacting the polymers with TESPIC. This modification of the polymers was essential to allow their chemical grafting on the AuMSS nanospheres. Subsequently, the AuMSS functionalization resulted in a size increase from 100±5 to 123±8, 152±9 and 160±27 nm for AuMSS+Polymer 25/75, 50/50 and 75/25, respectively. Besides, the increase of the PEOZ ratio also led to the neutralization of the AuMSS surface charges from -26.6±1.2 to -17.4±0.8 mV (AuMSS+Polymer 25/75), -14.2±0.2 (AuMSS+Polymer 50/50), and -7.2±0.8 mV (AuMSS+Polymer 75/25). The obtained size and surface charge values to AuMSS+Polymer nanospheres are still within the range considered ideal for their application in biological systems. On the other side, the nanoparticles cytocompatibility evaluation show a protective effect of the AuMSS polymeric coating. The AuMSS+Polymer 25/75, 50/50 and 75/25 nanospheres presented an increased biocompatibility, with cells displaying viability values superior to 70%, even when cells were seeded in contact with the highest concentration of nanoparticles (200 µg/mL). In addition, no significant alterations were observed in the HeLa cells motility after being incubated with AuMSS+Polymer 25/75, 50/50 and 75/25 nanospheres, at concentrations up to 200 µg/mL, for 72 h. On the other side, despite all AuMSS groups present a non-hemolytic nature at concentrations up to 200 µg/mL, the AuMSS+Polymer 50/50 and 75/25 nanospheres showed the lower hemolysis rate, with less than 1% of hemoglobin released. Finally, the uptake studies showed that the nanoparticles can be internalized by HeLa cells. The AuMSS nanospheres functionalization with PEOZ and β-CD increased the nanoparticles uptake, in comparison to non-coated AuMSS, in 136±15, 140±20, and 42±8% for the AuMSS+Polymer 25/75, 50/50 and 75/25 nanospheres. Therefore, the present findings encourage the further development of this simple multifunctional nanosystems for being applied in chemotherapy and bioimaging.

In the near future, the complete characterization of the drug loading and release profile at both physiological and acidic pH, as well as the evaluation of the antitumoral effect in 2D and 3D cell culture, will be essential to confirm the enhanced biological performance of the polymer coated AuMSS

nanospheres as well as their multifunctional potential. Then, the most promising formulation will proceed to *in vivo* assays to explore the polymers potential to improve the nanoparticles biodistribution and biosafety as well as to enhance the antitumoral effect.

Additionally, targeting moieties such as folate, transferrin, aptamers, and anti-bodies can be attached to the particle surface for increasing the AuMSS selectivity to cancer cells, towards an improved therapeutic outcome and ultimately enhancing the patients' life expectancy and well-being.

Chapter 5

References

5. References

1. Torre LA, Bray F, Siegel RL, Ferlay J, Lortet-Tieulent J, Jemal A. Global cancer statistics, 2012. CA Cancer J Clin. 2015;65(2):87-108.
2. Siegel RL, Miller KD, Jemal A. Cancer statistics, 2018. CA Cancer J Clin. 2018;68(1):7-30.
3. Miranda N GM, Andrade C, Santos G. Programa Nacional para as Doenças Oncológicas. Direção-Geral da Saúde 2017.
4. Vineis P, Wild CP. Global cancer patterns: causes and prevention. Lancet. 2014;383(9916):549-57.
5. Floor SL, Dumont JE, Maenhaut C, Raspe E. Hallmarks of cancer: of all cancer cells, all the time? Trends Mol Med. 2012;18(9):509-15.
6. Hanahan D, Weinberg RA. Hallmarks of cancer: the next generation. Cell. 2011;144(5):646-74.
7. Pietras K, Ostman A. Hallmarks of cancer: interactions with the tumor stroma. Exp Cell Res. 2010;316(8):1324-31.
8. Bussard KM, Mutkus L, Stumpf K, Gomez-Manzano C, Marini FC. Tumor-associated stromal cells as key contributors to the tumor microenvironment. Breast Cancer Research. 2016;18(1).
9. Barcellos-Hoff MH, Lyden D, Wang TC. The evolution of the cancer niche during multistage carcinogenesis. Nat Rev Cancer. 2013;13(7):511-8.
10. Cui Y, Guo G. Immunomodulatory Function of the Tumor Suppressor p53 in Host Immune Response and the Tumor Microenvironment. International Journal of Molecular Sciences. 2016;17(11).
11. Hanahan D, Weinberg RA. The hallmarks of cancer. Cell. 2000;100(1):57-70.
12. Rani B, Cao Y, Malfettone A, Tomuleasa C, Fabregat I, Giannelli G. Role of the tissue microenvironment as a therapeutic target in hepatocellular carcinoma. World J Gastroenterol. 2014;20(15):4128-40.
13. Giampazolias E, Tait SWG. Mitochondria and the hallmarks of cancer. Febs Journal. 2016;283(5):803-14.
14. Artandi SE, DePinho RA. Telomeres and telomerase in cancer. Carcinogenesis. 2010;31(1):9-18.
15. Goel HL, Mercurio AM. VEGF targets the tumour cell. Nat Rev Cancer. 2013;13(12):871-82.
16. Yadav L, Puri N, Rastogi V, Satpute P, Sharma V. Tumour Angiogenesis and Angiogenic Inhibitors: A Review. J Clin Diagn Res. 2015;9(6):XE01-XE5.
17. Canel M, Serrels A, Frame MC, Brunton VG. E-cadherin-integrin crosstalk in cancer invasion and metastasis. J Cell Sci. 2013;126(2):393-401.
18. DeSantis CE, Lin CC, Mariotto AB, Siegel RL, Stein KD, Kramer JL, et al. Cancer treatment and survivorship statistics, 2014. CA Cancer J Clin. 2014;64(4):252-71.
19. Hu QY, Sun WJ, Wang C, Gu Z. Recent advances of cocktail chemotherapy by combination drug delivery systems. Adv Drug Deliver Rev. 2016;98:19-34.
20. Holohan C, Van Schaeybroeck S, Longley DB, Johnston PG. Cancer drug resistance: an evolving paradigm. Nat Rev Cancer. 2013;13(10):714-26.

21. Links M, Brown R. Clinical relevance of the molecular mechanisms of resistance to anti-cancer drugs. Expert Rev Mol Med. 1999;1999:1-21.
22. Rebucci M, Michiels C. Molecular aspects of cancer cell resistance to chemotherapy. Biochem Pharmacol. 2013;85(9):1219-26.
23. Al-Lazikani B, Banerji U, Workman P. Combinatorial drug therapy for cancer in the post-genomic era. Nat Biotechnol. 2012;30(7):679-92.
24. Sharom FJ. Complex Interplay between the P-Glycoprotein Multidrug Efflux Pump and the Membrane: Its Role in Modulating Protein Function. Front Oncol. 2014;4:41.
25. Parhi P, Mohanty C, Sahoo SK. Nanotechnology-based combinational drug delivery: an emerging approach for cancer therapy. Drug Discov Today. 2012;17(17-18):1044-52.
26. Moreira AF, Gaspar VM, Costa EC, de Melo-Diogo D, Machado P, Paquete CM, et al. Preparation of end-capped pH-sensitive mesoporous silica nanocarriers for on-demand drug delivery. Eur J Pharm Biopharm. 2014;88(3):1012-25.
27. Cai ZL, Yook S, Lu YJ, Bergstrom D, Winnik MA, Pignol JP, et al. Local Radiation Treatment of HER2-Positive Breast Cancer Using Trastuzumab-Modified Gold Nanoparticles Labeled with Lu-177. Pharm Res-Dordr. 2017;34(3):579-90.
28. Mancini S, Minniti S, Gregori M, Sancini G, Cagnotto A, Couraud PO, et al. The hunt for brain Abeta oligomers by peripherally circulating multi-functional nanoparticles: Potential therapeutic approach for Alzheimer disease. Nanomedicine. 2016;12(1):43-52.
29. Ruff J, Huwel S, Kogan MJ, Simon U, Galla HJ. The effects of gold nanoparticles functionalized with ss-amyloid specific peptides on an in vitro model of blood-brain barrier. Nanomedicine. 2017;13(5):1645-52.
30. Hernando S, Herran E, Figueiro-Silva J, Pedraz JL, Igartua M, Carro E, et al. Intranasal Administration of TAT-Conjugated Lipid Nanocarriers Loading GDNF for Parkinson's Disease. Mol Neurobiol. 2018;55(1):145-55.
31. Yoo J, Lee E, Kim HY, Youn DH, Jung J, Kim H, et al. Electromagnetized gold nanoparticles mediate direct lineage reprogramming into induced dopamine neurons in vivo for Parkinson's disease therapy. Nat Nanotechnol. 2017;12(10):1006-14.
32. Moreira AF, Dias DR, Correia IJ. Stimuli-responsive mesoporous silica nanoparticles for cancer therapy: A review. Micropor Mesopor Mat. 2016;236:141-57.
33. Xu XY, Ho W, Zhang XQ, Bertrand N, Farokhzad O. Cancer nanomedicine: from targeted delivery to combination therapy. Trends in Molecular Medicine. 2015;21(4):223-32.
34. Albanese A, Tang PS, Chan WC. The effect of nanoparticle size, shape, and surface chemistry on biological systems. Annu Rev Biomed Eng. 2012;14:1-16.
35. Jia F, Liu X, Li L, Mallapragada S, Narasimhan B, Wang Q. Multifunctional nanoparticles for targeted delivery of immune activating and cancer therapeutic agents. J Control Release. 2013;172(3):1020-34.
36. Wicki A, Witzigmann D, Balasubramanian V, Huwyler J. Nanomedicine in cancer therapy: challenges, opportunities, and clinical applications. J Control Release. 2015;200:138-57.

37. Akbarzadeh A, Rezaei-Sadabady R, Davaran S, Joo SW, Zarghami N, Hanifehpour Y, et al. Liposome: classification, preparation, and applications. Nanoscale Res Lett. 2013;8(1):102.
38. Mehnert W, Mader K. Solid lipid nanoparticles: production, characterization and applications. Adv Drug Deliv Rev. 2001;47(2-3):165-96.
39. Wissing SA, Kayser O, Muller RH. Solid lipid nanoparticles for parenteral drug delivery. Adv Drug Deliv Rev. 2004;56(9):1257-72.
40. Kaur IP, Bhandari R, Bhandari S, Kakkar V. Potential of solid lipid nanoparticles in brain targeting. J Control Release. 2008;127(2):97-109.
41. Almeida AJ, Souto E. Solid lipid nanoparticles as a drug delivery system for peptides and proteins. Adv Drug Deliv Rev. 2007;59(6):478-90.
42. Elsabahy M, Wooley KL. Design of polymeric nanoparticles for biomedical delivery applications. Chem Soc Rev. 2012;41(7):2545-61.
43. Plummer R, Wilson RH, Calvert H, Boddy AV, Griffin M, Sludden J, et al. A Phase I clinical study of cisplatin-incorporated polymeric micelles (NC-6004) in patients with solid tumours. Br J Cancer. 2011;104(4):593-8.
44. Wijagkanalan W, Kawakami S, Hashida M. Designing dendrimers for drug delivery and imaging: pharmacokinetic considerations. Pharm Res. 2011;28(7):1500-19.
45. Frechet JM. Functional polymers and dendrimers: reactivity, molecular architecture, and interfacial energy. Science. 1994;263(5154):1710-5.
46. Kesharwani P, Jain K, Jain NK. Dendrimer as nanocarrier for drug delivery. Progress in Polymer Science. 2014;39(2):268-307.
47. Somani S, Blatchford DR, Millington O, Stevenson ML, Dufes C. Transferrin-bearing polypropylenimine dendrimer for targeted gene delivery to the brain. J Control Release. 2014;188:78-86.
48. Svenson S, Tomalia DA. Dendrimers in biomedical applications--reflections on the field. Adv Drug Deliv Rev. 2005;57(15):2106-29.
49. Lee CC, MacKay JA, Frechet JM, Szoka FC. Designing dendrimers for biological applications. Nat Biotechnol. 2005;23(12):1517-26.
50. Liong M, Lu J, Kovochich M, Xia T, Ruehm SG, Nel AE, et al. Multifunctional inorganic nanoparticles for imaging, targeting, and drug delivery. ACS Nano. 2008;2(5):889-96.
51. Nazir S, Hussain T, Ayub A, Rashid U, MacRobert AJ. Nanomaterials in combating cancer: therapeutic applications and developments. Nanomedicine. 2014;10(1):19-34.
52. Maier-Hauff K, Ulrich F, Nestler D, Niehoff H, Wust P, Thiesen B, et al. Efficacy and safety of intratumoral thermotherapy using magnetic iron-oxide nanoparticles combined with external beam radiotherapy on patients with recurrent glioblastoma multiforme. J Neurooncol. 2011;103(2):317-24.
53. Madani SY, Naderi N, Dissanayake O, Tan A, Seifalian AM. A new era of cancer treatment: carbon nanotubes as drug delivery tools. Int J Nanomedicine. 2011;6:2963-79.
54. Kumari P, Ghosh B, Biswas S. Nanocarriers for cancer-targeted drug delivery. J Drug Target. 2016;24(3):179-91.

55. Kemp JA, Shim MS, Heo CY, Kwon YJ. "Combo" nanomedicine: Co-delivery of multi-modal therapeutics for efficient, targeted, and safe cancer therapy. Adv Drug Deliv Rev. 2016;98:3-18.
56. Ernsting MJ, Murakami M, Roy A, Li SD. Factors controlling the pharmacokinetics, biodistribution and intratumoral penetration of nanoparticles. J Control Release. 2013;172(3):782-94.
57. Dixit S, Novak T, Miller K, Zhu Y, Kenney ME, Broome AM. Transferrin receptor-targeted theranostic gold nanoparticles for photosensitizer delivery in brain tumors. Nanoscale. 2015;7(5):1782-90.
58. Gaspar VM, Costa EC, Queiroz JA, Pichon C, Sousa F, Correia IJ. Folate-targeted multifunctional amino acid-chitosan nanoparticles for improved cancer therapy. Pharm Res. 2015;32(2):562-77.
59. Farokhzad OC, Langer R. Impact of nanotechnology on drug delivery. ACS Nano. 2009;3(1):16-20.
60. Vander Heiden MG, Cantley LC, Thompson CB. Understanding the Warburg effect: the metabolic requirements of cell proliferation. Science. 2009;324(5930):1029-33.
61. Lee ES, Gao Z, Bae YH. Recent progress in tumor pH targeting nanotechnology. J Control Release. 2008;132(3):164-70.
62. Gerweck LE, Seetharaman K. Cellular pH gradient in tumor versus normal tissue: potential exploitation for the treatment of cancer. Cancer Res. 1996;56(6):1194-8.
63. Popat A, Liu J, Lu GQ, Qiao SZ. A pH-responsive drug delivery system based on chitosan coated mesoporous silica nanoparticles. J Mater Chem. 2012;22(22):11173-8.
64. Swift T, Swanson L, Geoghegan M, Rimmer S. The pH-responsive behaviour of poly(acrylic acid) in aqueous solution is dependent on molar mass. Soft Matter. 2016;12(9):2542-9.
65. Wang ZH, Tian YF, Zhang H, Qin YM, Li D, Gan L, et al. Using hyaluronic acid-functionalized pH stimuli-responsive mesoporous silica nanoparticles for targeted delivery to CD44-overexpressing cancer cells. Int J Nanomed. 2016;11:6485-97.
66. Estrela JM, Ortega A, Obrador E. Glutathione in cancer biology and therapy. Crit Rev Clin Lab Sci. 2006;43(2):143-81.
67. Cheng R, Feng F, Meng F, Deng C, Feijen J, Zhong Z. Glutathione-responsive nano-vehicles as a promising platform for targeted intracellular drug and gene delivery. J Control Release. 2011;152(1):2-12.
68. Ganta S, Devalapally H, Shahiwala A, Amiji M. A review of stimuli-responsive nanocarriers for drug and gene delivery. J Control Release. 2008;126(3):187-204.
69. Li ZY, Hu JJ, Xu Q, Chen S, Jia HZ, Sun YX, et al. A redox-responsive drug delivery system based on RGD containing peptide-capped mesoporous silica nanoparticles. J Mater Chem B. 2015;3(1):39-44.
70. Sun JT, Piao JG, Wang LH, Javed M, Hong CY, Pan CY. One-pot synthesis of redox-responsive polymers-coated mesoporous silica nanoparticles and their controlled drug release. Macromol Rapid Commun. 2013;34(17):1387-94.
71. Xie Z, Gong H, Liu M, Zhu H, Sun H. The properties of mesoporous silica nanoparticles functionalized with different PEG-chain length via the disulfide bond linker and drug release in glutathione medium. J Biomater Sci Polym Ed. 2016;27(1):55-68.

72. Mo R, Jiang T, DiSanto R, Tai W, Gu Z. ATP-triggered anticancer drug delivery. Nat Commun. 2014;5:3364.
73. He X, Zhao Y, He D, Wang K, Xu F, Tang J. ATP-responsive controlled release system using aptamer-functionalized mesoporous silica nanoparticles. Langmuir. 2012;28(35):12909-15.
74. Lai J, Shah BP, Zhang Y, Yang L, Lee KB. Real-Time Monitoring of ATP-Responsive Drug Release Using Mesoporous-Silica-Coated Multicolor Upconversion Nanoparticles. ACS Nano. 2015;9(5):5234-45.
75. Dias DR, Moreira AF, Correia IJ. The effect of the shape of gold core-mesoporous silica shell nanoparticles on the cellular behavior and tumor spheroid penetration. J Mater Chem B. 2016;4(47):7630-40.
76. Moreira AF, Dias DR, Costa EC, Correia IJ. Thermo- and pH-responsive nano-in-micro particles for combinatorial drug delivery to cancer cells. Eur J Pharm Sci. 2017;104:42-51.
77. La-Beck NM, Gabizon AA. Nanoparticle Interactions with the Immune System: Clinical Implications for Liposome-Based Cancer Chemotherapy. Front Immunol. 2017;8:416.
78. Yildirimer L, Thanh NT, Loizidou M, Seifalian AM. Toxicology and clinical potential of nanoparticles. Nano Today. 2011;6(6):585-607.
79. Zhang L, Gu FX, Chan JM, Wang AZ, Langer RS, Farokhzad OC. Nanoparticles in medicine: therapeutic applications and developments. Clin Pharmacol Ther. 2008;83(5):761-9.
80. Bose T, Latawiec D, Mondal PP, Mandal S. Overview of nano-drugs characteristics for clinical application: the journey from the entry to the exit point. J Nanopart Res. 2014;16(8).
81. Hoshyar N, Gray S, Han HB, Bao G. The effect of nanoparticle size on in vivo pharmacokinetics and cellular interaction. Nanomedicine. 2016;11(6):673-92.
82. Mitragotri S, Burke PA, Langer R. Overcoming the challenges in administering biopharmaceuticals: formulation and delivery strategies. Nat Rev Drug Discov. 2014;13(9):655-72.
83. Bertrand N, Wu J, Xu X, Kamaly N, Farokhzad OC. Cancer nanotechnology: the impact of passive and active targeting in the era of modern cancer biology. Adv Drug Deliv Rev. 2014;66:2-25.
84. Chou LY, Ming K, Chan WC. Strategies for the intracellular delivery of nanoparticles. Chem Soc Rev. 2011;40(1):233-45.
85. Arami H, Khandhar A, Liggitt D, Krishnan KM. In vivo delivery, pharmacokinetics, biodistribution and toxicity of iron oxide nanoparticles. Chem Soc Rev. 2015;44(23):8576-607.
86. Mao ZW, Zhou XY, Gao CY. Influence of structure and properties of colloidal biomaterials on cellular uptake and cell functions. Biomater Sci-Uk. 2013;1(9):896-911.
87. Sahay G, Alakhova DY, Kabanov AV. Endocytosis of nanomedicines. J Control Release. 2010;145(3):182-95.
88. Pozzi D, Colapicchioni V, Caracciolo G, Piovesana S, Capriotti AL, Palchetti S, et al. Effect of polyethyleneglycol (PEG) chain length on the bio-nano-interactions between PEGylated lipid nanoparticles and biological fluids: from nanostructure to uptake in cancer cells. Nanoscale. 2014;6(5):2782-92.

89. Verhoef JJ, Carpenter JF, Anchordoquy TJ, Schellekens H. Potential induction of anti-PEG antibodies and complement activation toward PEGylated therapeutics. Drug Discov Today. 2014;19(12):1945-52.
90. Bauer M, Lautenschlaeger C, Kempe K, Tauhardt L, Schubert US, Fischer D. Poly(2-ethyl-2-oxazoline) as Alternative for the Stealth Polymer Poly(ethylene glycol): Comparison of in vitro Cytotoxicity and Hemocompatibility. Macromol Biosci. 2012;12(7):986-98.
91. Abu Lila AS, Nawata K, Shimizu T, Ishida T, Kiwada H. Use of polyglycerol (PG), instead of polyethylene glycol (PEG), prevents induction of the accelerated blood clearance phenomenon against long-circulating liposomes upon repeated administration. Int J Pharmaceut. 2013;456(1):235-42.
92. Nel AE, Madler L, Velegol D, Xia T, Hoek EM, Somasundaran P, et al. Understanding biophysicochemical interactions at the nano-bio interface. Nat Mater. 2009;8(7):543-57.
93. Blanco E, Shen H, Ferrari M. Principles of nanoparticle design for overcoming biological barriers to drug delivery. Nat Biotechnol. 2015;33(9):941-51.
94. Arnida, Janat-Amsbury MM, Ray A, Peterson CM, Ghandehari H. Geometry and surface characteristics of gold nanoparticles influence their biodistribution and uptake by macrophages. Eur J Pharm Biopharm. 2011;77(3):417-23.
95. Black KC, Wang Y, Luehmann HP, Cai X, Xing W, Pang B, et al. Radioactive 198Au-doped nanostructures with different shapes for in vivo analyses of their biodistribution, tumor uptake, and intratumoral distribution. ACS Nano. 2014;8(5):4385-94.
96. Hirn S, Semmler-Behnke M, Schleh C, Wenk A, Lipka J, Schaffler M, et al. Particle size-dependent and surface charge-dependent biodistribution of gold nanoparticles after intravenous administration. Eur J Pharm Biopharm. 2011;77(3):407-16.
97. Champion JA, Mitragotri S. Shape induced inhibition of phagocytosis of polymer particles. Pharm Res. 2009;26(1):244-9.
98. Yang X, Yang MX, Pang B, Vara M, Xia YN. Gold Nanomaterials at Work in Biomedicine. Chemical Reviews. 2015;115(19):10410-88.
99. Huang X, Jain PK, El-Sayed IH, El-Sayed MA. Plasmonic photothermal therapy (PPTT) using gold nanoparticles. Lasers Med Sci. 2008;23(3):217-28.
100. Huang XH, Jain PK, El-Sayed IH, El-Sayed MA. Gold nanoparticles: interesting optical properties and recent applications in cancer diagnostic and therapy. Nanomedicine. 2007;2(5):681-93.
101. Li N, Zhao PX, Astruc D. Anisotropic Gold Nanoparticles: Synthesis, Properties, Applications, and Toxicity. Angew Chem Int Edit. 2014;53(7):1756-89.
102. Huang X, El-Sayed MA. Gold nanoparticles: optical properties and implementations in cancer diagnosis and photothermal therapy. Journal of advanced research. 2010;1(1):13-28.
103. Cheng X, Sun R, Yin L, Chai Z, Shi H, Gao M. Light-Triggered Assembly of Gold Nanoparticles for Photothermal Therapy and Photoacoustic Imaging of Tumors In Vivo. Adv Mater. 2017;29(6).
104. Jing L, Liang X, Deng Z, Feng S, Li X, Huang M, et al. Prussian blue coated gold nanoparticles for simultaneous photoacoustic/CT bimodal imaging and photothermal ablation of cancer. Biomaterials. 2014;35(22):5814-21.

105. Lee SB, Lee HW, Singh TD, Li Y, Kim SK, Cho SJ, et al. Visualization of Macrophage Recruitment to Inflammation Lesions using Highly Sensitive and Stable Radionuclide-Embedded Gold Nanoparticles as a Nuclear Bio-Imaging Platform. Theranostics. 2017;7(4):926-34.
106. Li Z, Huang H, Tang S, Li Y, Yu XF, Wang H, et al. Small gold nanorods laden macrophages for enhanced tumor coverage in photothermal therapy. Biomaterials. 2016;74:144-54.
107. Sun M, Peng D, Hao H, Hu J, Wang D, Wang K, et al. Thermally Triggered in Situ Assembly of Gold Nanoparticles for Cancer Multimodal Imaging and Photothermal Therapy. ACS Appl Mater Interfaces. 2017;9(12):10453-60.
108. Love JC, Estroff LA, Kriebel JK, Nuzzo RG, Whitesides GM. Self-assembled monolayers of thiolates on metals as a form of nanotechnology. Chem Rev. 2005;105(4):1103-69.
109. Deng HH, Wang FF, Shi XQ, Peng HP, Liu AL, Xia XH, et al. Water-soluble gold nanoclusters prepared by protein-ligand interaction as fluorescent probe for real-time assay of pyrophosphatase activity. Biosens Bioelectron. 2016;83:1-8.
110. Liu J, Peng Q. Protein-gold nanoparticle interactions and their possible impact on biomedical applications. Acta Biomater. 2017;55:13-27.
111. Dreaden EC, Alkilany AM, Huang X, Murphy CJ, El-Sayed MA. The golden age: gold nanoparticles for biomedicine. Chem Soc Rev. 2012;41(7):2740-79.
112. Gupta A, Moyano DF, Parnsubsakul A, Papadopoulos A, Wang LS, Landis RF, et al. Ultrastable and Biofunctionalizable Gold Nanoparticles. ACS Appl Mater Interfaces. 2016;8(22):14096-101.
113. Chen YS, Frey W, Kim S, Homan K, Kruizinga P, Sokolov K, et al. Enhanced thermal stability of silica-coated gold nanorods for photoacoustic imaging and image-guided therapy. Opt Express. 2010;18(9):8867-78.
114. Jalani G, Cerruti M. Nano graphene oxide-wrapped gold nanostars as ultrasensitive and stable SERS nanoprobes. Nanoscale. 2015;7(22):9990-7.
115. del Pino P, Yang F, Pelaz B, Zhang Q, Kantner K, Hartmann R, et al. Basic Physicochemical Properties of Polyethylene Glycol Coated Gold Nanoparticles that Determine Their Interaction with Cells. Angew Chem Int Edit. 2016;55(18):5483-7.
116. Kreyling WG, Abdelmonem AM, Ali Z, Alves F, Geiser M, Haberl N, et al. In vivo integrity of polymer-coated gold nanoparticles. Nature Nanotechnology. 2015;10(7):619-23.
117. Zhang ZH, Liu CH, Bai JH, Wu CC, Xiao Y, Li YH, et al. Silver Nanoparticle Gated, Mesoporous Silica Coated Gold Nanorods (AuNR@MS@AgNPs): Low Premature Release and Multifunctional Cancer Theranostic Platform. Acs Appl Mater Inter. 2015;7(11):6211-9.
118. Abadeer NS, Brennan MR, Wilson WL, Murphy CJ. Distance and plasmon wavelength dependent fluorescence of molecules bound to silica-coated gold nanorods. ACS Nano. 2014;8(8):8392-406.
119. Li H, Tan LL, Jia P, Li QL, Sun YL, Zhang J, et al. Near-infrared light-responsive supramolecular nanovalve based on mesoporous silica-coated gold nanorods. Chem Sci. 2014;5(7):2804-8.
120. Mamaeva V, Sahlgren C, Linden M. Mesoporous silica nanoparticles in medicine--recent advances. Adv Drug Deliv Rev. 2013;65(5):689-702.
121. Colilla M, Baeza A, Vallet-Regí M. Mesoporous silica nanoparticles for drug delivery and controlled release applications. The Sol-Gel Handbook. 2015:1309-44.

122. Lu J, Liong M, Zink JI, Tamanoi F. Mesoporous silica nanoparticles as a delivery system for hydrophobic anticancer drugs. Small. 2007;3(8):1341-6.
123. Slowing II, Trewyn BG, Giri S, Lin VSY. Mesoporous silica nanoparticles for drug delivery and biosensing applications. Adv Funct Mater. 2007;17(8):1225-36.
124. Chen JC, Zhang RY, Han L, Tu B, Zhao DY. One-pot synthesis of thermally stable gold@mesoporous silica core-shell nanospheres with catalytic activity. Nano Res. 2013;6(12):871-9.
125. Kanehara M, Watanabe Y, Teranishi T. Thermally stable silica-coated hydrophobic gold nanoparticles. J Nanosci Nanotechnol. 2009;9(1):673-5.
126. Ghosh Chaudhuri R, Paria S. Core/shell nanoparticles: classes, properties, synthesis mechanisms, characterization, and applications. Chem Rev. 2012;112(4):2373-433.
127. Song JT, Yang XQ, Zhang XS, Yan DM, Wang ZY, Zhao YD. Facile Synthesis of Gold Nanospheres Modified by Positively Charged Mesoporous Silica, Loaded with Near-Infrared Fluorescent Dye, for in Vivo X-ray Computed Tomography and Fluorescence Dual Mode Imaging. ACS Appl Mater Interfaces. 2015;7(31):17287-97.
128. Kobayashi Y, Correa-Duarte MA, Liz-Marzan LM. Sol-gel processing of silica-coated gold nanoparticles. Langmuir. 2001;17(20):6375-9.
129. Liu SH, Han MY. Synthesis, functionalization, and bioconjugation of monodisperse, silica-coated gold nanoparticles: Robust bioprobes. Adv Funct Mater. 2005;15(6):961-7.
130. Mine E, Yamada A, Kobayashi Y, Konno M, Liz-Marzan LM. Direct coating of gold nanoparticles with silica by a seeded polymerization technique. J Colloid Interf Sci. 2003;264(2):385-90.
131. Caruso F, Spasova M, Saigueirino-Maceira V, Liz-Marzan LM. Multilayer assemblies of silica-encapsulated gold nanoparticles on decomposable colloid templates. Advanced Materials. 2001;13(14):1090-4.
132. Pastoriza-Santos I, Perez-Juste J, Liz-Marzan LM. Silica-coating and hydrophobation of CTAB-stabilized gold nanorods. Chem Mater. 2006;18(10):2465-7.
133. Ahmed S, Annu, Ikram S, Yudha SS. Biosynthesis of gold nanoparticles: A green approach. J Photoch Photobio B. 2016;161:141-53.
134. Dung TN, Kim DJ, Kim KS. Controlled synthesis and biomolecular probe application of gold nanoparticles. Micron. 2011;42(3):207-27.
135. Zhao PX, Li N, Astruc D. State of the art in gold nanoparticle synthesis. Coordin Chem Rev. 2013;257(3-4):638-65.
136. Murakami T, Tsuchida K. Recent advances in inorganic nanoparticle-based drug delivery systems. Mini Rev Med Chem. 2008;8(2):175-83.
137. Ferrier RC, Gines G, Gasparutto D, Pepin-Donat B, Rannou P, Composto RJ. Tuning Optical Properties of Functionalized Gold Nanorods through Controlled Interactions with Organic Semiconductors. J Phys Chem C. 2015;119(31):17899-909.
138. Yasun E, Li CM, Barut I, Janvier D, Qiu LP, Cui C, et al. BSA modification to reduce CTAB induced nonspecificity and cytotoxicity of aptamer-conjugated gold nanorods. Nanoscale. 2015;7(22):10240-8.

139. DuChene JS, Niu WX, Abendroth JM, Sun Q, Zhao WB, Huo FW, et al. Halide Anions as Shape-Directing Agents for Obtaining High-Quality Anisotropic Gold Nanostructures. Chem Mater. 2013;25(8):1392-9.
140. Scarabelli L, Coronado-Puchau M, Giner-Casares JJ, Langer J, Liz-Marzan LM. Monodisperse Gold Nanotriangles: Size Control, Large-Scale Self-Assembly, and Performance in Surface-Enhanced Raman Scattering. Acs Nano. 2014;8(6):5833-42.
141. Pelaz B, Grazu V, Ibarra A, Magen C, del Pino P, de la Fuente JM. Tailoring the synthesis and heating ability of gold nanoprisms for bioapplications. Langmuir. 2012;28(24):8965-70.
142. Tian F, Bonnier F, Casey A, Shanahan AE, Byrne HJ. Surface enhanced Raman scattering with gold nanoparticles: effect of particle shape. Anal Methods-Uk. 2014;6(22):9116-23.
143. Lohse SE, Murphy CJ. The Quest for Shape Control: A History of Gold Nanorod Synthesis. Chem Mater. 2013;25(8):1250-61.
144. Chandra K, Culver KSB, Werner SE, Lee RC, Odom TW. Manipulating the Anisotropic Structure of Gold Nanostars using Good's Buffers. Chem Mater. 2016;28(18):6763-9.
145. Xia XH, Xia YN. Gold nanocages as multifunctional materials for nanomedicine. Front Phys-Beijing. 2014;9(3):378-84.
146. Epifani M, Carlino E, Blasi C, Giannini C, Tapfer L, Vasanelli L. Sol-gel processing of Au nanoparticles in bulk 10% B2O3-90% SiO2 glass. Chem Mater. 2001;13(5):1533-9.
147. Chen YS, Frey W, Kim S, Kruizinga P, Homan K, Emelianov S. Silica-Coated Gold Nanorods as Photoacoustic Signal Nanoamplifiers. Nano Lett. 2011;11(2):348-54.
148. Hua Y, Chandra K, Dam DH, Wiederrecht GP, Odom TW. Shape-Dependent Nonlinear Optical Properties of Anisotropic Gold Nanoparticles. J Phys Chem Lett. 2015;6(24):4904-8.
149. Argyo C, Weiss V, Brauchle C, Bein T. Multifunctional Mesoporous Silica Nanoparticles as a Universal Platform for Drug Delivery. Chem Mater. 2014;26(1):435-51.
150. Hembury M, Chiappini C, Bertazzo S, Kalber TL, Drisko GL, Ogunlade O, et al. Gold-silica quantum rattles for multimodal imaging and therapy. P Natl Acad Sci USA. 2015;112(7):1959-64.
151. Liu J, Detrembleur C, De Pauw-Gillet MC, Mornet S, Jerome C, Duguet E. Gold Nanorods Coated with Mesoporous Silica Shell as Drug Delivery System for Remote Near Infrared Light-Activated Release and Potential Phototherapy. Small. 2015;11(19):2323-32.
152. Sreejith S, Joseph J, Nguyen KT, Murukeshan VM, Lye SW, Zhao YL. Graphene Oxide Wrapping of Gold-Silica Core-Shell Nanohybrids for Photoacoustic Signal Generation and Bimodal Imaging. Chemnanomat. 2015;1(1):39-45.
153. Chen Y, Chen HR, Zeng DP, Tian YB, Chen F, Feng JW, et al. Core/Shell Structured Hollow Mesoporous Nanocapsules: A Potential Platform for Simultaneous Cell Imaging and Anticancer Drug Delivery. Acs Nano. 2010;4(10):6001-13.
154. Terentyuk G, Panfilova E, Khanadeev V, Chumakov D, Genina E, Bashkatov A, et al. Gold nanorods with a hematoporphyrin-loaded silica shell for dual-modality photodynamic and photothermal treatment of tumors in vivo. Nano Res. 2014;7(3):325-37.

155. Wang SJ, Huang P, Nie LM, Xing RJ, Liu DB, Wang Z, et al. Single Continuous Wave Laser Induced Photodynamic/Plasmonic Photothermal Therapy Using Photosensitizer-Functionalized Gold Nanostars. Advanced Materials. 2013;25(22):3055-61.
156. Yang JP, Shen DK, Zhou L, Li W, Li XM, Yao C, et al. Spatially Confined Fabrication of Core-Shell Gold Nanocages@Mesoporous Silica for Near-Infrared Controlled Photothermal Drug Release. Chem Mater. 2013;25(15):3030-7.
157. Castillo RR, Colilla M, Vallet-Regi M. Advances in mesoporous silica-based nanocarriers for co-delivery and combination therapy against cancer. Expert Opin Drug Deliv. 2017;14(2):229-43.
158. Cole LE, Ross RD, Tilley JMR, Vargo-Gogola T, Roeder RK. Gold nanoparticles as contrast agents in x-ray imaging and computed tomography. Nanomedicine. 2015;10(2):321-41.
159. Li W, Chen X. Gold nanoparticles for photoacoustic imaging. Nanomedicine (Lond). 2015;10(2):299-320.
160. Gao B, Xu J, He KW, Shen L, Chen H, Yang HJ, et al. Cellular Uptake and Intra-Organ Biodistribution of Functionalized Silica-Coated Gold Nanorods. Mol Imaging Biol. 2016;18(5):667-76.
161. Thakor AS, Luong R, Paulmurugan R, Lin FI, Kempen P, Zavaleta C, et al. The fate and toxicity of Raman-active silica-gold nanoparticles in mice. Sci Transl Med. 2011;3(79):79ra33.
162. Zeng Q, Zhang Y, Ji W, Ye W, Jiang Y, Song J. Inhibitation of cellular toxicity of gold nanoparticles by surface encapsulation of silica shell for hepatocarcinoma cell application. ACS Appl Mater Interfaces. 2014;6(21):19327-35.
163. Lee KS, El-Sayed MA. Dependence of the enhanced optical scattering efficiency relative to that of absorption for gold metal nanorods on aspect ratio, size, end-cap shape, and medium refractive index. J Phys Chem B. 2005;109(43):20331-8.
164. Chen NT, Tang KC, Chung MF, Cheng SH, Huang CM, Chu CH, et al. Enhanced plasmonic resonance energy transfer in mesoporous silica-encased gold nanorod for two-photon-activated photodynamic therapy. Theranostics. 2014;4(8):798-807.
165. Hu B, Zhang LP, Chen XW, Wang JH. Gold nanorod-covered kanamycin-loaded hollow SiO2 (HSKAu(rod)) nanocapsules for drug delivery and photothermal therapy on bacteria. Nanoscale. 2013;5(1):246-52.
166. Liu W, Zhu Z, Deng K, Li Z, Zhou Y, Qiu H, et al. Gold nanorod@chiral mesoporous silica core-shell nanoparticles with unique optical properties. J Am Chem Soc. 2013;135(26):9659-64.
167. Monem AS, Elbialy N, Mohamed N. Mesoporous silica coated gold nanorods loaded doxorubicin for combined chemo-photothermal therapy. Int J Pharm. 2014;470(1-2):1-7.
168. Zhou H, Xu H, Li X, Lv Y, Ma T, Guo S, et al. Dual targeting hyaluronic acid - RGD mesoporous silica coated gold nanorods for chemo-photothermal cancer therapy. Mater Sci Eng C Mater Biol Appl. 2017;81:261-70.
169. Liu Y, Lv X, Liu J, Sun YQ, Guo W. Construction of a selective fluorescent probe for GSH based on a chloro-functionalized coumarin-enone dye platform. Chemistry. 2015;21(12):4747-54.

170. Lee C, Hwang HS, Lee S, Kim B, Kim JO, Oh KT, et al. Rabies Virus-Inspired Silica-Coated Gold Nanorods as a Photothermal Therapeutic Platform for Treating Brain Tumors. Adv Mater. 2017;29(13):1605563.
171. de Melo-Diogo D, Pais-Silva C, Dias DR, Moreira AF, Correia IJ. Strategies to Improve Cancer Photothermal Therapy Mediated by Nanomaterials. Adv Healthc Mater. 2017;6(10):1700073.
172. Hemmer E, Benayas A, Legare F, Vetrone F. Exploiting the biological windows: current perspectives on fluorescent bioprobes emitting above 1000 nm. Nanoscale Horiz. 2016;1(3):168-84.
173. Zhang Z, Wang L, Wang J, Jiang X, Li X, Hu Z, et al. Mesoporous silica-coated gold nanorods as a light-mediated multifunctional theranostic platform for cancer treatment. Adv Mater. 2012;24(11):1418-23.
174. Shen S, Tang H, Zhang X, Ren J, Pang Z, Wang D, et al. Targeting mesoporous silica-encapsulated gold nanorods for chemo-photothermal therapy with near-infrared radiation. Biomaterials. 2013;34(12):3150-8.
175. Seo SH, Kim BM, Joe A, Han HW, Chen X, Cheng Z, et al. NIR-light-induced surface-enhanced Raman scattering for detection and photothermal/photodynamic therapy of cancer cells using methylene blue-embedded gold nanorod@SiO2 nanocomposites. Biomaterials. 2014;35(10):3309-18.
176. Luo GF, Chen WH, Lei Q, Qiu WX, Liu YX, Cheng YJ, et al. A Triple-Collaborative Strategy for High-Performance Tumor Therapy by Multifunctional Mesoporous Silica-Coated Gold Nanorods. Adv Funct Mater. 2016;26(24):4339-50.
177. Chen J, Wiley B, Li ZY, Campbell D, Saeki F, Cang H, et al. Gold nanocages: engineering their structure for biomedical applications. Advanced materials. 2005;17(18):2255-61.
178. Wang Z, Chen Z, Liu Z, Shi P, Dong K, Ju E, et al. A multi-stimuli responsive gold nanocage-hyaluronic platform for targeted photothermal and chemotherapy. Biomaterials. 2014;35(36):9678-88.
179. Sun Y, Xia Y. Mechanistic study on the replacement reaction between silver nanostructures and chloroauric acid in aqueous medium. J Am Chem Soc. 2004;126(12):3892-901.
180. Khlebtsov BN, Khanadeev VA, Panfilova EV, Inozemtseva OA, Burov AM, Khlebtsov NG. A simple Mie-type model for silica-coated gold nanocages. Journal of Quantitative Spectroscopy and Radiative Transfer. 2013;121:23-9.
181. Cobley CM, Chen J, Cho EC, Wang LV, Xia Y. Gold nanostructures: a class of multifunctional materials for biomedical applications. Chem Soc Rev. 2011;40(1):44-56.
182. Khlebtsov B, Panfilova E, Khanadeev V, Bibikova O, Terentyuk G, Ivanov A, et al. Nanocomposites containing silica-coated gold-silver nanocages and Yb-2,4-dimethoxyhematoporphyrin: multifunctional capability of IR-luminescence detection, photosensitization, and photothermolysis. ACS Nano. 2011;5(9):7077-89.
183. Khlebtsov BN, Tuchina ES, Khanadeev VA, Panfilova EV, Petrov PO, Tuchin VV, et al. Enhanced photoinactivation of Staphylococcus aureus with nanocomposites containing plasmonic particles and hematoporphyrin. J Biophotonics. 2013;6(4):338-51.

184. Hu F, Zhang Y, Chen G, Li C, Wang Q. Double-walled Au nanocage/SiO2 nanorattles: integrating SERS imaging, drug delivery and photothermal therapy. Small. 2015;11(8):985-93.
185. Pallavicini P, Cabrini E, Borzenkov M, Sironi L, Chirico G. Applications of Gold Nanostars: Nanosensing, Thermal Therapy, Delivery Systems. Gold Nanostars: Springer; 2015. p. 43-59.
186. Atta S, Tsoulos TV, Fabris L. Shaping gold nanostar electric fields for surface-enhanced raman spectroscopy enhancement via silica coating and selective etching. The Journal of Physical Chemistry C. 2016;120(37):20749-58.
187. Harmsen S, Huang R, Wall MA, Karabeber H, Samii JM, Spaliviero M, et al. Surface-enhanced resonance Raman scattering nanostars for high-precision cancer imaging. Sci Transl Med. 2015;7(271):271ra7.
188. Fales AM, Yuan H, Vo-Dinh T. Silica-coated gold nanostars for combined surface-enhanced Raman scattering (SERS) detection and singlet-oxygen generation: a potential nanoplatform for theranostics. Langmuir. 2011;27(19):12186-90.
189. Li X, Xing L, Zheng K, Wei P, Du L, Shen M, et al. Formation of Gold Nanostar-Coated Hollow Mesoporous Silica for Tumor Multimodality Imaging and Photothermal Therapy. ACS Appl Mater Interfaces. 2017;9(7):5817-27.
190. An J, Yang XQ, Cheng K, Song XL, Zhang L, Li C, et al. In Vivo Computed Tomography/Photoacoustic Imaging and NIR-Triggered Chemo-Photothermal Combined Therapy Based on a Gold Nanostar-, Mesoporous Silica-, and Thermosensitive Liposome-Composited Nanoprobe. ACS Appl Mater Interfaces. 2017;9(48):41748-59.
191. Hainfeld JF, Slatkin DN, Focella TM, Smilowitz HM. Gold nanoparticles: a new X-ray contrast agent. Brit J Radiol. 2006;79(939):248-53.
192. Jain S, Hirst DG, O'Sullivan JM. Gold nanoparticles as novel agents for cancer therapy. Brit J Radiol. 2012;85(1010):101-13.
193. Pasternak JJ, Williamson EE. Clinical Pharmacology, Uses, and Adverse Reactions of Iodinated Contrast Agents: A Primer for the Non-radiologist. Mayo Clin Proc. 2012;87(4):390-402.
194. Kobayashi Y, Inose H, Nagasu R, Nakagawa T, Kubota Y, Gonda K, et al. X-ray imaging technique using colloid solution of Au/silica/poly(ethylene glycol) nanoparticles. Mater Res Innov. 2013;17(7):507-14.
195. van Schooneveld MM, Cormode DP, Koole R, van Wijngaarden JT, Calcagno C, Skajaa T, et al. A fluorescent, paramagnetic and PEGylated gold/silica nanoparticle for MRI, CT and fluorescence imaging. Contrast Media Mol Imaging. 2010;5(4):231-6.
196. Kircher MF, de la Zerda A, Jokerst JV, Zavaleta CL, Kempen PJ, Mittra E, et al. A brain tumor molecular imaging strategy using a new triple-modality MRI-photoacoustic-Raman nanoparticle. Nat Med. 2012;18(5):829.
197. Ramasamy M, Lee JH, Lee J. Development of gold nanoparticles coated with silica containing the antibiofilm drug cinnamaldehyde and their effects on pathogenic bacteria. Int J Nanomedicine. 2017;12:2813-28.

198. He Q, Zhang J, Shi J, Zhu Z, Zhang L, Bu W, et al. The effect of PEGylation of mesoporous silica nanoparticles on nonspecific binding of serum proteins and cellular responses. Biomaterials. 2010;31(6):1085-92.
199. Li YJ, Yan B. Photophysical properties of a novel organic-inorganic hybrid material: Eu(III)-beta-diketone complex covalently bonded to SiO(2) /ZnO composite matrix. Photochem Photobiol. 2010;86(5):1008-15.
200. O'Brien J, Wilson I, Orton T, Pognan F. Investigation of the Alamar Blue (resazurin) fluorescent dye for the assessment of mammalian cell cytotoxicity. Eur J Biochem. 2000;267(17):5421-6.
201. Yildirim A, Ozgur E, Bayindir M. Impact of mesoporous silica nanoparticle surface functionality on hemolytic activity, thrombogenicity and non-specific protein adsorption. J Mater Chem B. 2013;1(14):1909-20.
202. Bernd A, Ott M, Ishikawa H, Schroten H, Schwerk C, Fricker G. Characterization of efflux transport proteins of the human choroid plexus papilloma cell line HIBCPP, a functional in vitro model of the blood-cerebrospinal fluid barrier. Pharm Res-Dordr. 2015;32(9):2973-82.
203. Konradi R, Pidhatika B, Muhlebach A, Textor M. Poly-2-methyl-2-oxazoline: a peptide-like polymer for protein-repellent surfaces. Langmuir. 2008;24(3):613-6.
204. Mero A, Pasut G, Dalla Via L, Fijten MW, Schubert US, Hoogenboom R, et al. Synthesis and characterization of poly(2-ethyl 2-oxazoline)-conjugates with proteins and drugs: suitable alternatives to PEG-conjugates? J Control Release. 2008;125(2):87-95.
205. Koshkina O, Westmeier D, Lang T, Bantz C, Hahlbrock A, Wurth C, et al. Tuning the Surface of Nanoparticles: Impact of Poly(2-ethyl-2-oxazoline) on Protein Adsorption in Serum and Cellular Uptake. Macromol Biosci. 2016;16(9):1287-300.
206. Zalipsky S, Hansen CB, Oaks JM, Allen TM. Evaluation of blood clearance rates and biodistribution of poly(2-oxazoline)-grafted liposomes. J Pharm Sci. 1996;85(2):133-7.
207. Nichols JW, Bae YH. Odyssey of a cancer nanoparticle: from injection site to site of action. Nano Today. 2012;7(6):606-18.
208. Ou H, Cheng T, Zhang Y, Liu J, Ding Y, Zhen J, et al. Surface-adaptive zwitterionic nanoparticles for prolonged blood circulation time and enhanced cellular uptake in tumor cells. Acta Biomater. 2018;65:339-48.
209. Wang Q, Shen M, Zhao T, Xu Y, Lin J, Duan Y, et al. Low toxicity and long circulation time of polyampholyte-coated magnetic nanoparticles for blood pool contrast agents. Sci Rep. 2015;5:7774.
210. Xiao W, Lin J, Li M, Ma Y, Chen Y, Zhang C, et al. Prolonged in vivo circulation time by zwitterionic modification of magnetite nanoparticles for blood pool contrast agents. Contrast Media Mol Imaging. 2012;7(3):320-7.
211. Yoo JW, Chambers E, Mitragotri S. Factors that Control the Circulation Time of Nanoparticles in Blood: Challenges, Solutions and Future Prospects. Curr Pharm Design. 2010;16(21):2298-307.
212. Gidwani B, Vyas A. A Comprehensive Review on Cyclodextrin-Based Carriers for Delivery of Chemotherapeutic Cytotoxic Anticancer Drugs. Biomed Res Int. 2015;2015.

213. Lakkakula JR, Macedo Krause RW. A vision for cyclodextrin nanoparticles in drug delivery systems and pharmaceutical applications. Nanomedicine (Lond). 2014;9(6):877-94.
214. Shelley H, Babu RJ. Role of Cyclodextrins in Nanoparticle-Based Drug Delivery Systems. J Pharm Sci. 2018;107(7):1741-53.
215. Colombo A, Gherardi F, Goidanich S, Delaney JK, de la Rie ER, Ubaldi MC, et al. Highly transparent poly(2-ethyl-2-oxazoline)-TiO2 nanocomposite coatings for the conservation of matte painted artworks. Rsc Adv. 2015;5(103):84879-88.
216. Sambasevam KP, Mohamad S, Sarih NM, Ismail NA. Synthesis and Characterization of the Inclusion Complex of beta-cyclodextrin and Azomethine. International Journal of Molecular Sciences. 2013;14(2):3671-82.
217. Rosenholm JM, Sahlgren C, Linden M. Towards multifunctional, targeted drug delivery systems using mesoporous silica nanoparticles - opportunities & challenges. Nanoscale. 2010;2(10):1870-83.
218. Li SD, Huang L. Pharmacokinetics and biodistribution of nanoparticles. Mol Pharm. 2008;5(4):496-504.
219. Chen Y, Huang Y, Qin D, Liu W, Song C, Lou K, et al. beta-Cyclodextrin-Based Inclusion Complexation Bridged Biodegradable Self-Assembly Macromolecular Micelle for the Delivery of Paclitaxel. PLoS One. 2016;11(3):e0150877.
220. Gaspar VM, Goncalves C, de Melo-Diogo D, Costa EC, Queiroz JA, Pichon C, et al. Poly(2-ethyl-2-oxazoline)-PLA-g-PEI amphiphilic triblock micelles for co-delivery of minicircle DNA and chemotherapeutics. J Control Release. 2014;189:90-104.
221. He C, Hu Y, Yin L, Tang C, Yin C. Effects of particle size and surface charge on cellular uptake and biodistribution of polymeric nanoparticles. Biomaterials. 2010;31(13):3657-66.
222. Slowing I, Trewyn BG, Lin VS. Effect of surface functionalization of MCM-41-type mesoporous silica nanoparticles on the endocytosis by human cancer cells. J Am Chem Soc. 2006;128(46):14792-3.
223. Lingappan N, Kim DH, Park JM, Lim KT. Water soluble graphene oxide/poly(1-vinylimidazole) composites: synthesis and characterization. J Nanosci Nanotechnol. 2014;14(8):5713-7.
224. Rachmawati H, Edityaningrum CA, Mauludin R. Molecular inclusion complex of curcumin-beta-cyclodextrin nanoparticle to enhance curcumin skin permeability from hydrophilic matrix gel. AAPS PharmSciTech. 2013;14(4):1303-12.
225. Chan MH, Lin HM. Preparation and identification of multifunctional mesoporous silica nanoparticles for in vitro and in vivo dual-mode imaging, theranostics, and targeted tracking. Biomaterials. 2015;46:149-58.
226. Rapido F. The potential adverse effects of haemolysis. Blood Transfus. 2017;15(3):218-21.
227. Khullar P, Singh V, Mahal A, Dave PN, Thakur S, Kaur G, et al. Bovine Serum Albumin Bioconjugated Gold Nanoparticles: Synthesis, Hemolysis, and Cytotoxicity toward Cancer Cell Lines. J Phys Chem C. 2012;116(15):8834-43.
228. Lu F, Wu SH, Hung Y, Mou CY. Size effect on cell uptake in well-suspended, uniform mesoporous silica nanoparticles. Small. 2009;5(12):1408-13.